Elsevier Editorial System(tm) for Cold Regions Science and Technology
Manuscript Draft

Manuscript Number: CRST-D-15-00255R2

Title: Characterization of summer Arctic sea ice morphology in the 135°-175°W sector using multi-scale methods

Article Type: Research Paper

Keywords: Sea ice; concentration; thickness; melt pond; morphology; Arctic

Corresponding Author: Dr. Ruibo Lei, Ph.D.

Corresponding Author's Institution: Polar Research Institute of China

First Author: Ruibo Lei, Ph.D.

Order of Authors: Ruibo Lei, Ph.D.; Xiangshan Tian-Kunze, Dr.; Bingrui Li, Dr.; Petra Heil, Dr.; Jia Wang, Dr.; Junbao Zeng; Zhongxiang Tian, Dr.

Abstract: In summer 2014, sea ice morphological characteristics were investigated in the 135°-175°W sector of the Arctic Ocean using in situ, shipborne, and remote sensing measurements. Sea ice in this sector was deformed and compact compared to previous observations. The average ice area in the region (70°-82.5°N, 135°-175°W) was 7.6×105 km2 for 29 July through 6 September 2014, the fourth largest record between 2003-2014. This can be attributed to the enhanced multiyear sea ice inflow from north of the Canadian Arctic Archipelago from September 2013 to August 2014. Multiyear ice coverage in the study region on 30 April 2014 was 55%, which was larger than the values in 2005-2013. During the melt season of 2014, the Arctic Dipole had a positive anomaly, associated with enhanced southerly wind. In summer 2014 the marginal ice zone exhibited a distinct ice retreat, whereas the pack ice zone (PIZ) showed strong persistence due to the large coverage of multiyear ice. The northward retreat of the PIZ boundary was less than 100 km from late July through early September 2014. In the PIZ of 76-80.5°N, average ice thickness weighted by ice concentration, obtained by shipborne measurements in August 2014 was 0.54 m thicker than that obtained in August 2010 due to enhenced ice deformation and less open waters in 2014. At 81°N, sea ice with modal thickness of 1.48 m reached thermodynamic balance by late August 2014, which was much earlier than that in 2010.

***Cover Letter**

Dear Dr. Juerg Schweizer,

We would like to submit a second revised manuscript named by "Characterization of summer Arctic sea ice morphology in the 135°–175°W sector using multi-scale methods" [CRST-D-15-00255R1] to Cold Regions Science and Technology. According to the comments from you and reviewers, we made a revision for the manuscript by carrying out the tasks given below: (a) revise some figures, and (b) make the expression cleaner.

Please find the following files in our submission package:
1. The manuscripts (DOC file) with tracked changes,
and 2. Responses to the comments of reviewers.

Thank you for your time.

Sincerely,
Ruibo Lei, other co-authors

*Response to Reviewers

Reply to the Reviewer

1 line 9-11, the sentence "combined with …" seems not needed, can be deleted. If you want to keep, I suggest to change "these indicated" to "it is found"
We modified this expression (Page 2-Line 9-10).

2 line 13, add "and properties" behind the information.
We added it according to the suggestion. (Page 3-Line 13)

3 line20-21, the sentence "for Hs+i about …." is not clear, please rewrite it.
We rewrote it. (Page 8-Line 20-21)

4 fig 1, caption, spell out SS, LS, MIZ, PIZ.
We spelled out these abbreviations in the caption of Fig. 1. (Page 6-Line 8-9)

5 figure 4, I would still think it is important to identify two modes from the EM31 for a, b, d, f in the figure, since these may well represent two different types of sea ice. The majority level ice (first peak) and secondary level ice (second peak). Then relative text in page 14 and 15 should be revised there. the line 11-16 of page 15 about the two modes are basically right. But it is not accurate since the some regions has only one mode, some regions mode values are not as said there are 0.5-0.6, and 1.0-1.3
We identified two modes from the ice thickness shown in this figure and modified the related expression. (Figure 4, Page 14-15)

6 figure 7, I believe the outlines of melt ponds in d is not quite right. I hope you can make exactly outline of melt ponds based on figure 2. Based on my reading of the figures, I believe the EM31 underestimate ice thickness for both ridge and melt pond. Please check and revise the text if I am right. It is interesting to see the change in sea ice thickness from 19th to 25th, but it is not shown any result here. I hope it can be added.
(1) We made the outlines of melt ponds shown in Fig. 7d more correct.
(2) Yes, the EM31 underestimate ice thickness for both ridge and melt pond. We revised the related text. (Page 19-Line 14-15, Page 20, Line 1-3)
(3) Both the average value and spatial distribution of sea ice thicknesses obtained from 19 and 25 August did not show identifiable change as shown below. To save the space, we don't want to show this fig in the paper, but add some descriptions on this measurement. (Page 20, Line 5-6)

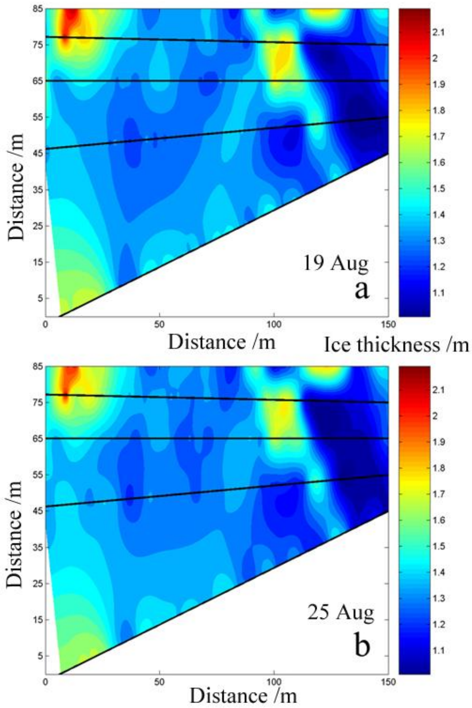

Sea ice thickness distribution on 19 and 25 August

Characterization of summer Arctic sea ice morphology in the 135°–175°W sector using multi-scale methods

Ruibo Lei [a,*], Xiangshan Tian-Kunze[b], Bingrui Li[a], Petra Heil[c], Jia Wang[d], Junbao Zeng[e], Zhongxiang Tian[f]

[a] *Key Laboratory for Polar Science of the State Oceanic Administration, Polar Research Institute of China, Shanghai, 200136, China*

[b] *Institute of Oceanography, University of Hamburg, Hamburg, 20146, Germany*

[c] *Australian Antarctic Division and Antarctic Climate and Ecosystems Cooperative Research Centre, University of Tasmania, Private Bag 80, Hobart, Tasmania, 7001, Australia*

[d] *NOAA Great Lakes Environmental Research Laboratory, Ann Arbor, MI 48108,USA*

[e] *Shenyang Institute of Automation, Chinese Academy of Sciences, Shenyang, Liaoning, 110016,China*

[f] *National Marine Environmental Forecasting Center, Beijing, 100081,China*

***Corresponding author** at: Key Laboratory for Polar Science of the State Oceanic Administration, Polar Research Institute of China, Shanghai 200136, China

Fax: +86-21-58711663; Tel: +86-21-58714974.

E-mail address: leiruibo@pric.org.cn (R. Lei).

Highlights

- **Summer Arctic sea ice morphology has been measured using multi-scale methods**
- **The PSA had compact sea ice in summer 2014 due to year-round negative AO**
- **Larger winter ice inflow and less summer melt induced earlier refreezing in 2014**

ABSTRACT

In summer 2014, sea ice morphological characteristics were investigated in the 135°–175°W sector of the Arctic Ocean using *in situ*, shipborne, and remote sensing measurements. Sea ice in this sector was deformed and compact compared to previous observations. The average ice area in the region (70°–82.5°N, 135°–175°W) was 7.6×10^5 km^2 for 29 July through 6 September 2014, the fourth largest record between 2003–2014. This can be attributed to the enhanced multiyear sea ice inflow from north of the Canadian Arctic Archipelago from September 2013 to August 2014. Multiyear ice coverage in the study region on 30 April 2014 was 55%, which was larger than the values in 2005–2013. During the melt season of 2014, the Arctic Dipole had a positive anomaly, associated with enhanced southerly wind. In summer 2014 the marginal ice zone exhibited a distinct ice retreat, whereas the pack ice zone (PIZ) showed strong persistence due to the large coverage of multiyear ice. The northward retreat of the PIZ boundary was less than 100 km from late July through early September 2014. In the PIZ of 76–80.5°N, average ice thickness weighted by ice concentration, obtained by shipborne measurements in August 2014 was 0.54 m thicker than that obtained in August 2010 due to enhenced ice deformation and less open waters in 2014. At 81°N, sea ice with modal thickness of 1.48 m reached thermodynamic balance by late August 2014, which was much earlier than that in 2010.

Key words: Sea ice; concentration; thickness; melt pond; morphology; Arctic

1 Introduction

Arctic Sea ice has declined rapidly during the last three decades, as substantiated by the reductions in sea ice extent (Xia et al., 2014) and thickness (Kwok and Rothrock, 2009), loss of multiyear ice coverage (Comiso, 2012) and total ice volume (Laxon et al, 2013). The most significant decline of summer Arctic sea ice extent occurred in the Pacific sector from the Beaufort Sea to East Siberian Sea (Xia et al., 2014), due to the enhanced positive polarity of the Arctic Dipole Anomaly (DA) (Wang et al., 2009), the increased Pacific inflow (Shimada et al., 2006), and the ice albedo feedback (Perovich et al., 2008). Sea ice area in this sector has substantial interannual variability caused by atmospheric circulation (Wei et al., 2014), and the reduced summer ice cover contributes significantly to the decrease in the Arctic multiyear ice coverage (Kowk and Cunningham, 2010).

Spaceborne sensors deliver Arctic-wide sea ice information and properties. Sea ice concentration data have been availble since the late 1970s, with higher resolution data, derived from the Advanced Microwave Scanning Radiometer onboard EOS (AMSR-E) and its successor (AMSR2), available from June 2002 through October 2011 and from July 2012 onwards. Using the algorithm of ARTIST Sea Ice (ASI) (Spreen et al., 2008), the University of Bremen provides AMRS-E and AMSR2 ice concentrations with consistent grid resolution of 6.25×6.25 km^2. Under clear sky conditions, the MODerate-resolution Imaging Spectroradiometer (MODIS) provides optical imagery at a spatial resolution of 250 m × 250 m. However, because of limitations due to cloud cover, MODIS cannot provide sustained data for sea ice charting. The laser altimeter onboard ICESat and radar altimeter onboard CryoSat-2 provide ice freeboard data from 2003 to 2008 (intermittently) and 2010 onwards, respectively. However, because of surface melt, spaceborne altimeter cannot accurately measure the ice freeboard during summer.

Shipborne observations give a snapshot of the spatial distributions of sea ice morphological parameters, including concentration, thickness, and surface features, at local to regional scales. These observations can provide a larger perspective than *in situ* observations, while detecting small-scale features that are not resolved by satellite measurements. Therefore, they are a bridge between satellite and *in situ* observations. In the Southern Ocean, the protocol of the Antarctic Sea Ice Processes and Climate program (ASPeCt) has been used to systematically record sea ice morphology since the 1990s (Worby and Allison, 1999). Similar to the ASPeCt, the protocol of the Arctic Shipborne Sea Ice Standardization Tool (ASSIST) was established by the Climate-Cryosphere Arctic Sea Ice Working Group, to characterize typical Arctic conditions, e.g., surface melt pond and impurity concentrations. Its quantization of sea ice concentration is the same as that in ASPeCt and it provides output conforming to the World Meteorology Organization (WMO) "egg code". Sustained data records collected using consistent observational methods are propitious to identify long-term change. For example, many marine science voyages have covered the Pacific sector of the Arctic Ocean since 1994 (e.g., Lei et al., 2012a; Li et al., 2005; Lu et al., 2010; Perovich et al., 2009; Tucker et al., 1999; Xie et al., 2013). Most of these cruises took place between late July and early September. Prior to 2010 the ASPeCt protocol was used to observe underway sea ice morphology, whereas the ASSIST protocol was used since 2010.

Dynamic interactions between sea ice and ocean are strongly dependent on sea ice bottom morphology. The geometrical parameters of the ice ridge are the dominant factors for the ice-ocean drag coefficient (Lu et al., 2011). When the weathering of sea ice surface is advanced, the sail depth, and hence the thickness of deformed ice is difficult to estimate by visual observation (Tin and Jeffries, 2003). An electromagnetic-inductive (EM) sounding instrument suspended beyond the icebreaker can overcome this problem (Haas, 1998). Furthermore, ground-based EM can measure sea ice thickness with higher spatial resolution than shipborne EM (Xie et al., 2013). However, it still cannot provide data of ice surface and bottom morphology separately. Upward looking sonar (ULS) onboard an underwater vehicle can map ice bottom morphology at high spatial resolution (Williams et al., 2014). Thus, combined using of both *in situ* measurements of EM and ULS is a good method to completely characterize sea ice morphology.

The sixth Chinese National Arctic Research Expedition was conducted using R/V *Xuelong* in summer 2014 (CHINARE-2014). Shipborne observations of sea ice morphology were made in the Pacific sector of the Arctic Ocean from late July through early September 2014. *In situ* EM and ULS measurements were made at several ice stations. In the present study, we combined the data from *in situ* and spaceborne measurements to give a full picture of summer sea ice morphology in the study region, from floe to basin scales. The data collected in 2014 were compared with historical data obtained by shipborne and spaceborne measurements, to determine interannual variability and responses to changes of atmospheric circulations.

2 Methods and data

2.1 Overview of CHINARE-2014

During the CHINARE-2014, the R/V *Xuelong* entered the Arctic sea ice zone north of Alaska on 29 July 2014 (Fig. 1). The vessel traversed in 155°–170°W before entering the pack ice zone (PIZ) at 76.2°N/167.0°W on 8 August 2014. Five short-term stations (SS) of 3 to 8 h duration were conducted within the PIZ, covering the region around the Chukchi Cap, to characterize sea ice physics. Following SS 5, the vessel continued northward into the Canadian Basin to 80.8°N, 157.6°W (point I), where a long-term station (LS) was set up on 17 August 2014.

On 26 August 2014, following 9 days at the LS, the vessel navigated southward, stopping for SS 6 and 7 on 28 August 2014. The vessel entered the marginal ice zone (MIZ) at 76.1°N, 143.5°W on 30 August 2014, within which it navigated westward and then exited into open water on 6 September 2014 (Fig.1, point L). we defined the various legs along the vessel's track according to turning points, with A–I and J–L for the northward and southward trajectories, respectively.

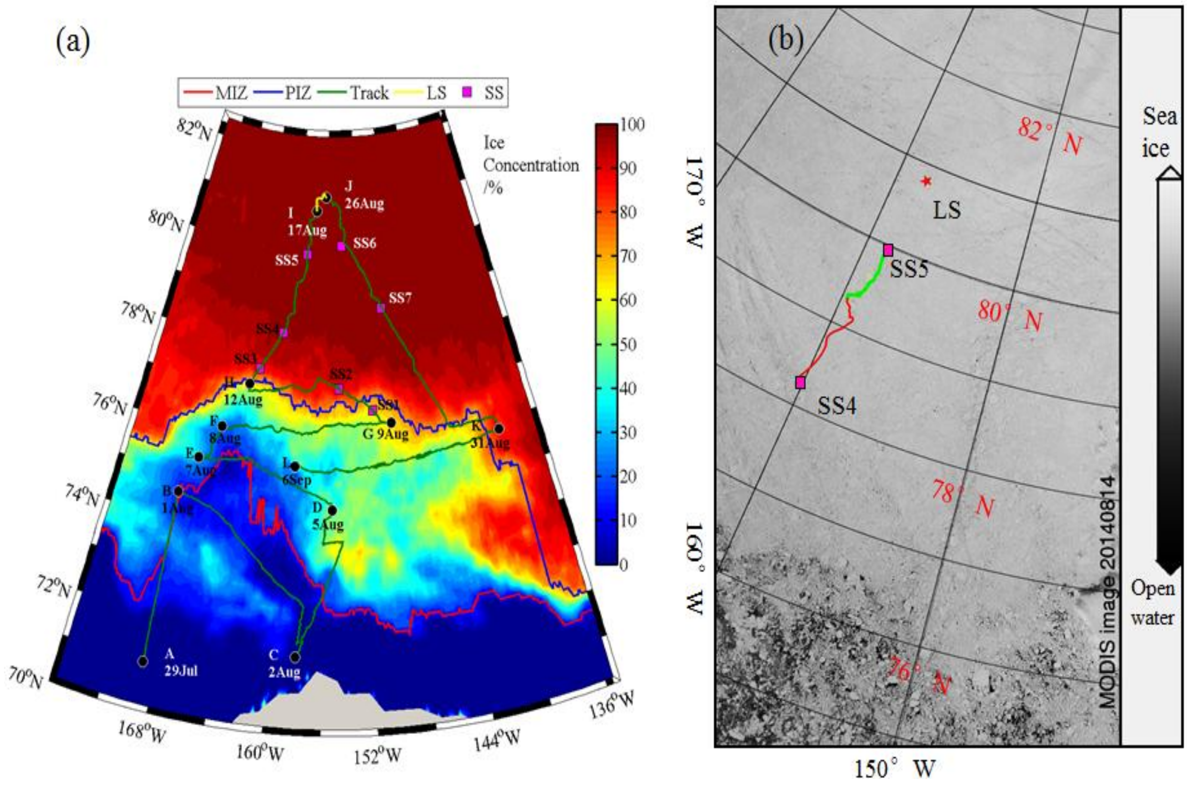

Fig. 1 (a) Average sea ice concentration derived from AMSR2 data, from 29 July to 6 September 2014, with the trajectory of the *Xuelong* (green) and its turning points (black dots, A–L), locations of short-term station (SS, purple square) and long-term station (LS, yellow line), southern boundary of the marginal ice zone (red), and pack ice zone (blue). (b) Optical imagery from MODIS on 14 August 2014, with the ship trajectory on 14 (red) and 15(green) August, plus locations of SS 4, SS 5, and LS.

2.2 Shipborne measurements

An EM31-ICE (9.8 kHz, Geonics) was mounted over the vessel's port side, about 15 m back from the bow to avoid data contamination by ice cracks formed by the vessel itself. The EM31 together with a GPS receiver (Jupiter 32, Navman), ultrasonic ranging sensor (SR50A, Campbell), and laser altimeter (LDM42.2, Jenoptik) were fixed in a fiberglass-reinforced frame, to enable stable deployment to a height of 4.0 m above waterline and 8.0 m beyond the ship's hull. Both the ultrasonic ranger and laser altimeter were used to measure the distance between the instrument and snow/water surface (H_L). The accuracies of the ultrasonic sensor and the laser are ± 0.01 m and ± 0.005 m, respectively. The EM31 measured the apparent conductivity (δ) in the vertically magnetic dipole mode. At both, LS and SS 6, the distance between the system and ice surface was varied from 4.0 m to 0.0 m, in 0.10 m steps to obtain the altitude dependency of δ. Total thicknesses of snow and sea ice (H_{s+i}) at five representative sites within the EM31 footprint were obtained from boreholes. Using 41 pairs of δ and distance between the sensor and ice-water interface (H_{EM}), an empirical relationship of H_{s+i} varying as a function of δ and H_L was then established as:

$$H_{s+i}=11.027-\mathrm{LN}(\delta-9.01)/0.578-H_L. \quad (1)$$

The fit deviation is 0.15±0.15 m (or 10%±10%), which is significant at the 0.05 confidence level. In most cases, the laser records were used to determine H_L. In cases when the laser pointing was over open water, data from the sonic sensor were used. During passage within ice zone, the vessel's speed averaged 3–10 knots. This means that the ship moved 1.6–5.2 m between two samples of the EM31. Kovacs et al. (1995) estimated that the footprint diameter for a vertically magnetic dipole mode is ~ 1.3 times the EM antenna height above the ice-water interface. With a distance between the EM31 and ice-water interface of ~5.5 m, the footprint is ~ 7.2 m. Therefore, this system cannot resolve the high-frequency variability of ice bottom morphology. Data acquired when the vessel stopped was excluded from the analysis. A cutoff of 0.1 m in H_{s+i} was used to identify open water, because of relatively large uncertainties in the EM31 measurements over very thin ice.

Half-hourly ASSIST observations were conducted at the bridge of the R/V *Xuelong* to document sea ice concentration, sea ice and snow thickness, fractions (the area ratio relative to sea ice) of melt ponds, dirty ice (with severe impurity depositions) and ridging, and floe size. Sea ice concentration was only assessed for a local area with a diameter of 2 km, which might be reduced to less than 1 km on foggy days. Sea ice thickness was estimated through scaling the thickness of overturning ice block with a buoy suspended near the waterline. This method is well suited to measure the thickness of level ice but not ice ridges because, upon being turned over, the ice ridges often disintegrate (Tin and Jeffries, 2003). Surface temperatures of water or sea ice were measured by a downward looking infrared thermometer (KT19.82, Heitronics), with an accuracy of ±0.2°C. The thermometer was mounted off vessel's port side at a height of 4.0 m above the waterline and 2 m from the outermost surface of the vessel's hull, hence ensuring that the vessel's hull is outside the instrument footprint. The measurement of surface temperature was used to identify the melt stage of ice surface. Visual observation of sea ice morphology and surface temperature measurements were carried out throughout the campaign. Measurements of ice thickness using the EM31 are available from 31 July to 31 August 2014.

2.3 *In situ* measurements

At each SS, we occupied a representative thickness profile of 50–200 m length over visually level sea ice. Along this profile, the EM31 was placed directly on the snow surface in the vertically magnetic dipole mode. Because the H_{s+i} was about 1.5 m, the footprint for the ground-based EM31 measurements was estimated at about 2.0 m. This measurement, associated with recording snow depth, was done every 1 m. Snow and sea ice thicknesses were measured via boreholes every 10 m along the same profile. Coincident EM31 and borehole measurements from all SS were used to derive the empirical relationship between H_{s+i} and δ:

$$H_{s+i}=12.851-\mathrm{LN}(\delta)/0.438. \quad (2)$$

The best fit distance is 0.13±0.10 m (or 8%±6%), significant at the 0.01 confidence level. Sea ice thickness (H_i) at all EM measurement sites was then acquired by subtracting snow depth (H_s) from H_{s+i}.

At LS, a quasi-trapezoidal area was set out for sea ice thickness and snow depth measurement by EM31 and borehole (Area 1 in Fig. 2). Along five profiles of 150 m within this area, H_{s+i} and H_s was measured using the EM31 and a snow ruler every 1 m, and H_s, H_i, and freeboard (H_f) were obtained by borehole every 10 m. On 19 August 2014, both borehole and EM31 measurements were made. EM31 measurement was repeated on 25 August 2014.

Another area with a size about 100 m × 100 m (Area 2 in Fig. 2) was outlined to measure sea ice draft (H_d) using an Autonomous and Remotely operated underwater Vehicle (ARV). A floe-referenced navigational coordinate system was defined. To measure H_d, the mission was preprogrammed and the trajectory was pre-set to comb-like prior to the ARV launch. An inertial navigation system, comprising an Octans-1000 fiber optic gyro (IXSEA) and a Doppler velocity log (DVL, Teledyne RD Instruments), was used to obtain the ARV position relative to the ice. Rotation of the floe was measured by dual GPS on the surface, with real-time data sent to the underwater control system. The DVL, assembled with four sonic transducers, was also used as an ULS to measure the distance to the ice bottom. The beam angle of each transducer was 3.6°. During the measurements, the ARV navigated at a depth of ~ 6 m below the waterline. With ice draft of 1.5 m, the footprint diameter for each beam under the ice base was ~ 0.3 m. The distance to the ice base was obtained by averaging measurements of the four transducers. H_d was acquired by subtracting this distance from navigation depth. ULS measurements had an interval of 0.1 m along the track. The ARV was launched three times at the LS between 21 and 23 August 2014, with measurement areas 100 m × 37.8 m, 99.2 m × 87.9 m, and 99.7 m × 86.7 m, respectively.

In addition, two transects from the ARV launch hole, with lengths 180 m (P1) and 130 m (P2), were defined for comparisons among the ULS, EM and borehole measurements (Fig. 2). On 22 August 2014, the ULS, EM31, and borehole measurements were taken along the transects at intervals 0.1, 1, and 10 m, respectively. The ULS measurements were done along both the forward and backward navigations. Along the P1, there was a melt pond 68–80 m from the launch hole. Surface measurements could not be made there.

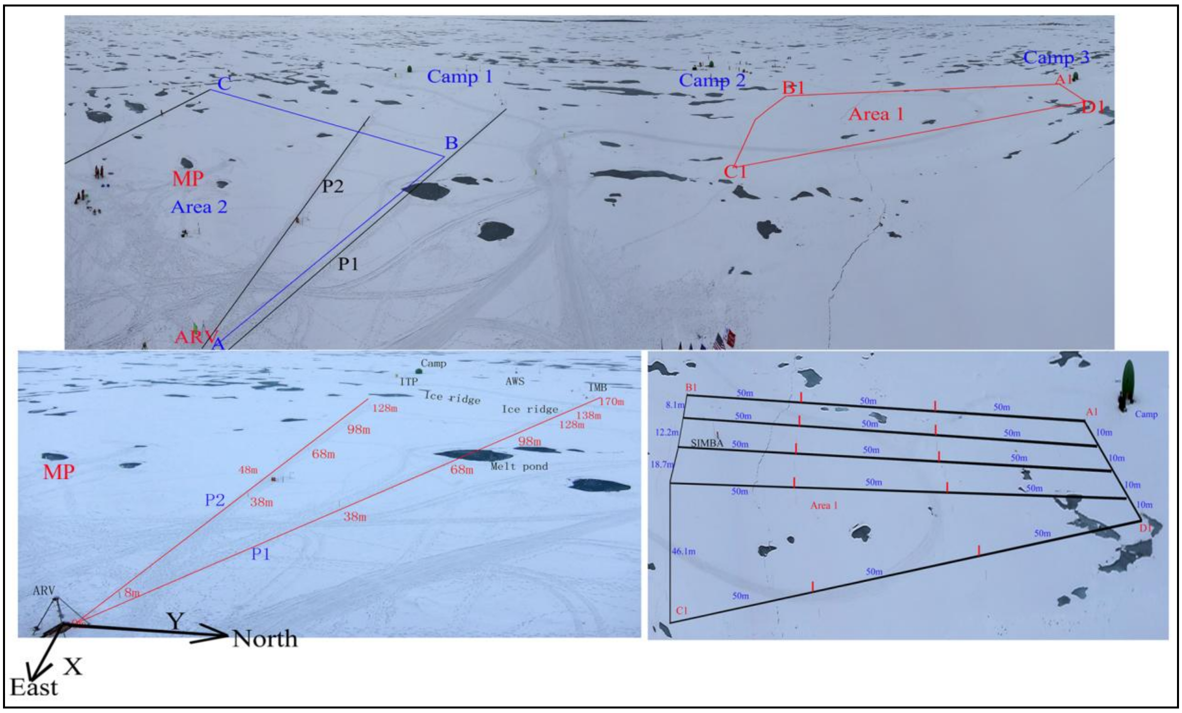

Fig. 2 Measurement areas by borehole and EM31 in Area 1, by ULS in Area 2, and by borehole, EM31 and ULS along P1 and P2. Dark patches are melt ponds (MP).

2.4 Remotely sensed data

The CHINARE-2014 cruise trajectory set the study domain: 70°–82.5°N, 135°–175°W, and the study period from 29 July to 6 September. Daily AMSR-E/AMSR2 ASI ice concentration data (6.25×6.25 km^2) were used to track the evolution of the 2003–2014 sea ice area across the domain. Thresholds of 15% and 75% ice concentration were used to define the southern boundaries of the MIZ and PIZ. Interannual variabilities were determined for the average sea ice area and the average MIZ and PIZ boundaries from 29 July through 6 September. In addition, a MODIS imagery with 250-m resolution on 14 August 2014 was used to visually characterize spatial distributions of sea ice conditions (Fig. 1b). To explore the relationship between interannual variabilities of sea ice in the study domain and those in the entire Arctic Ocean, we calculated Arctic-wide sea ice extent averaged in the same period and used annual minimum Arctic sea ice extent determined by the Special Sensor Microwave/Imager (SSM/I) data (Fetterer et al., 2002).

At the basin scale, sea ice morphological characteristics depend mainly on the coverage of multiyear ice. Sea ice classes can be assigned from atmospherically corrected SSM/I brightness temperatures and advanced scatterometer data (Eastwood, 2012). Data of sea ice type are compiled and archived by the Norwegian Meteorological Service Ocean and Sea Ice Satellite Application Facility (OSI-SAF) system, available from 2005 to present during the freezing period through 30 April each year. GPS data from ice-tethered buoys can be used to characterize sea ice advection. Here, we combined the data of OSI-SAF ice type on 30 April 2014 and GPS data from 30 April through 6 September 2014 measured by nine Ice-Tethered Profilers (ITP), to extrapolate the coverage of multiyear ice in the study domain during the summer. The ITP data were provided by the Woods Hole Oceanographic Institution. The sea ice classes in 2014 were compared with those from 2005 to 2013.

2.5 Auxiliary data

Besides the CHINARE-2014, shipborne observations of eight other cruises in the Pacific section of the Arctic Ocean from 1994 to 2012 were used to characterize the interannual variability. Two of the cruises were transpolar, including the Arctic Ocean Section in 1994 (AOS94) (Tucker et al., 1999) and Healy Oden TRans-Arctic eXpedition in 2005

(HOTRAX05) (Perovich et al., 2009). Shipborne sea ice observations have been done during each CHINARE cruise since 2003 (Lei et al., 2012a; Li et al., 2005; Xie et al., 2013). Data collected in the study domain during the summers of 2003, 2008, 2010, and 2012 were used here. In addition, two ASSIST archived cruises coincide with our study domain. These were Canadian Coast Guard *St. Laurent* voyages in the summers 2006 and 2012.

NCEP/NCAR Reanalysis (Kistler et al., 2001) sea level air pressure for north of 70°N from 2003 to 2014 was used for empirical orthogonal function (EOF) analysis. The Arctic Oscillation (AO) and DA correspond to the first and second leading EOF modes (Wu et al., 2006). We analyzed empirical relationships between sea ice in the study domain and AO/DA indices to determine the responses of interannual variability of sea ice to atmospheric circulation patterns.

3 Results

3.1 Sea ice morphology along ship track

In the MIZ from A (71.0°N) to F (76.2°N), both sea ice concentration and H_{s+i} from visual observations showed large spatial variability, ranging 0–90% and 0.3–1.7 m, respectively (Fig. 3). Measurements of shipborne EM31 ranged from 0.1 to 3.7 m, with an average of 0.92±0.45 m, which was much larger than that from visual observation (0.68±0.31 m). The deviation between two measurements can be attributed to their contrasting ability to identify ice ridges. The fraction of ice ridge in the MIZ was extensive, because most level ice had already melted.

After entering the PIZ, sea ice concentration increased rapidly from point F to G, and then remained above 70%. North of SS4 (14 August, 78.3°N), ice concentration increased to > 90%. Accordingly, H_{s+i} from visual observations increased from a bin of 0.4–1.4 m around point F to a bin of 1.1–2.0 m upon approaching the LS (80.8°N). A distinct change in the EM31 measurements occurred around SS4. North of this station, all thin ice was contained in narrow leads due to the refreezing. As the widths of most leads in the region were smaller than the horizontal resolution of EM31, the EM31 did not detect any thin ice with $H_{s+i} < 0.2$ m there. Half-hourly averaged EM31 data increased from a range of 0.4–1.5 m near F to a range of 1.1–1.3 m near the LS.

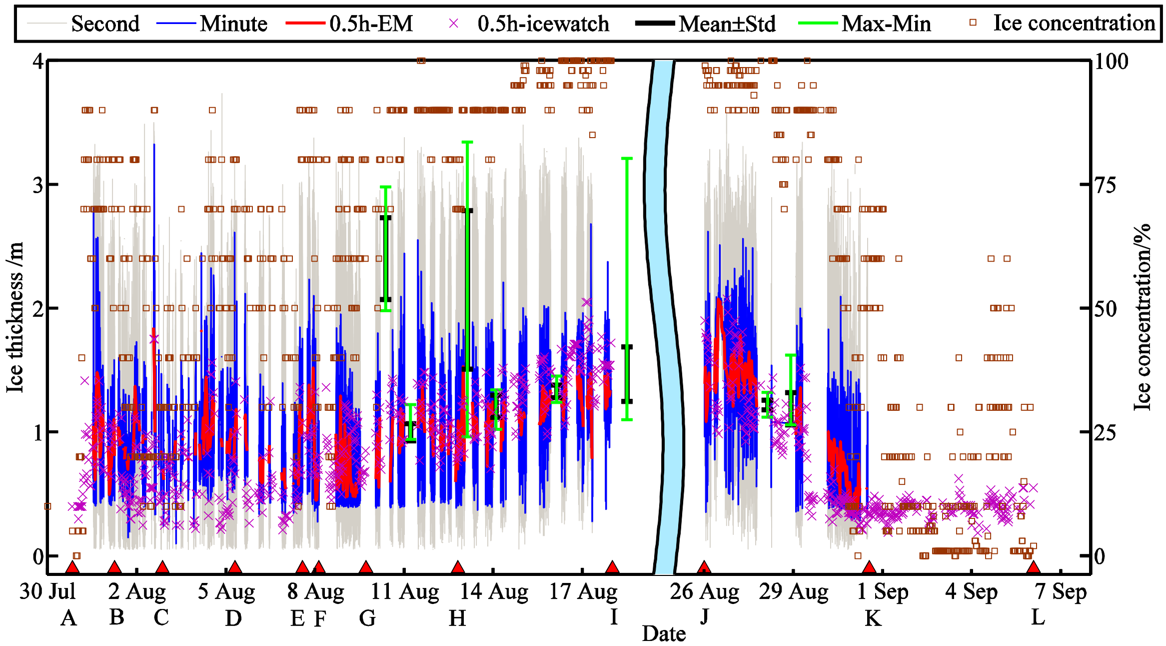

Fig. 3 Variations of sea ice (+ snow) thickness measured by shipborne EM31 (grey) and its minute and half-hourly averages (blue and red), from visual observation (purple), and EM31 at ice stations (black and green). Sea ice concentration from the visual observation (brown); light blue strip is temporal gap during the LS.

The sea ice concentration remained above 75% as the ship moved southward from the LS to 77.4°N. From there the concentration decreased gradually. South of SS7, the ship departed the PIZ and reentered the MIZ. There, ice thickness decreased gradually. By 31 August 2014 (76.1°N), H_{s+i} from both visual observations and half-hourly average EM31 data decreased to 0.2–0.4 m. From points K to L, the visually observed ice concentration showed great spatial change, from 0 to 70%, whereas the visually observed H_{s+i} remained low (0.2–

0.6 m). This implies that the ice in this region was liklely subject to completely melt by early September.

In situ EM31 measurements confirmed that the transects at SS 2, 4, 5 and 6 were on level ice. Along these transects, the maximum-minimum difference of thickness as well as twice the standard deviation were less than 0.3 m. At SS1, SS3, LS, and SS7, although the ice surface appeared level, thickness measurements indicated that the floes were deformed. Weathering was the most likely reason for the smoothing of the upper surface. The maximum-minimum difference of H_{s+i} at the aforementioned stations was 0.7–2.0 m.

To characterize sea ice thickness probability distribution, the domain was divided into 5 sub regions: Region 1 from points A to F, the MIZ along the northward track; Region 2 from point F to SS4, the southern PIZ along the northward track; Region 3 from SS4 to point I, the northern PIZ along the northward track; Region 4 from point J to SS7, the PIZ along the southward track; and Region 5 from SS7 to point K, the MIZ along the southward track. Many ice ridges but very little thin ice was identified by EM31 in Region 1 (Fig. 4a). In Region 2, ice concentration increased sharply compared with that in Region 1 (77.4% vs. 51.5%), whereas, average ice thickness measured by the EM31 was nearly the same as that in Region 1 (0.90 m vs. 0.92 m). This deviation was due to the larger contribution of level ice effectively lowering the overall ice thickness in Region 2. There were distinct modes can be identified in the sea ice thickness ditribution obtained by EM measurement is this region, withe one centering at 0.50 m related to thin ice and the other centering at 1.10 related to level ice. The mode related to thin ice was more outstanding than that identified in Region 1. The overall averages from the EM31 and visual observations were consistent (0.90 m vs. 0.99 m) in Region 2. In Region 3, average ice concentration increased to 96.5%, and the ice thickness increased too. The EM31 recorded very little thin ice, winthout mode in thikness distribution can identified for this ice type. The mode of level ice determined by the EM31 was much smaller than that by visual observations (1.20 m vs. 1.60 m). We suspect that this was due to relatively thin ice surrounding melt ponds. This thin ice was easily missed by the visual observation, while melt pond coverage was relatively large in this region (~20%). Compared with Region 3, the range of modal peak for the ice thickness distribution was much broader in Region 4, which were 1.1–1.8 m and 1.4–2.0 m for the visual and EM31 measurements, respectively. In this region, ice ridge coverage was greater, but melt pond coverage was smaller than in Region 3. Consequently, the contributions of level ice and ice ridges to the probability distribution of ice thickness in Region 4 were mixed, resulting in the wider range of modal ice. In Region 5, average ice concentration declined remarkably to 56.9%, comparable to that in Region 1. However, the average ice thickness obtained by EM31 was 0.68 m in this region, which was much thinner than that in Region 1 (0.92 m). In the region from K to L, the mode related to thin ice was more outstanding than that frin SS7 to K, and very few ice thicker than 0.75 m can be identified. Using data from the entire campaign, the average ice thickness obtained from visual observations was 0.94 m, comparable to the averaged EM31 data (1.03 m). Two obvious modal peaks can be identified from both datasets, which centred at 0.5–0.6 m for thin ice and 1.0–1.3 m for level ice, respectively. The distinct difference is that the EM measurement detects more thick ice (with thickness > 2 m). Consequently, the probability distribution of EM observed ice thickness was much wider than that obained by visual observation.

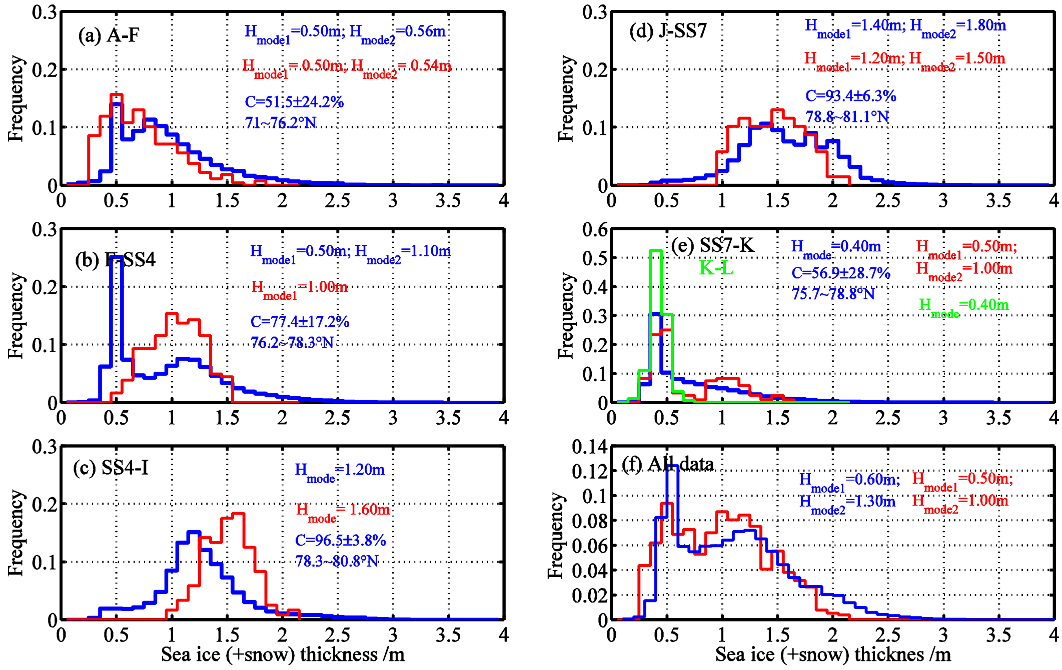

Fig. 4 Frequency distributions of H_{s+i} in various regions (a–e) and that obtained from all data (f) of shipborne EM31 (blue) and visual observations (red and green); H_{mode} and C denote modal of H_{s+i} and ice concentration.

According to spatial change in surface air temperature (Fig. 5a) and associated with a large amount of open water encountered there, south of 72.5°N along the northward track, surface temperature of ice/ocean was relatively high, ranging 3.0–6.0 °C (Fig. 5b). Even on sea ice, surface temperature can reach above –1.8°C because of the formation of melt ponds, where it was generally fresh water. Further north, surface temperature of ice/ocean decreased as ice concentration increased (Fig. 5c). Upon entering the PIZ, surface temperature decreased further to −6.0° – +1.5 °C. In the PIZ along the northward trajectory, maximum melt pond fraction reached 30% (Fig. 5d). Assuming an albedo of 0.3, 0.7, and 0.1 for melt pond, sea ice, and open water according to Lei et al. (2016), respectively, and ice concentration of 95%, reductions of regional average albedo by melt ponds and open water are 17% and 4%, respectively. Thus, melt ponds had much greater impact on the reduction of albedo than open water in this region. In contrast to the northward track, along the southward trajectory spatial variability of surface temperature was much less in both, the PIZ and the MIZ, ranging −3.0° – +1.0 °C. Surface temperature rarely reached above 0°C as refreezing.

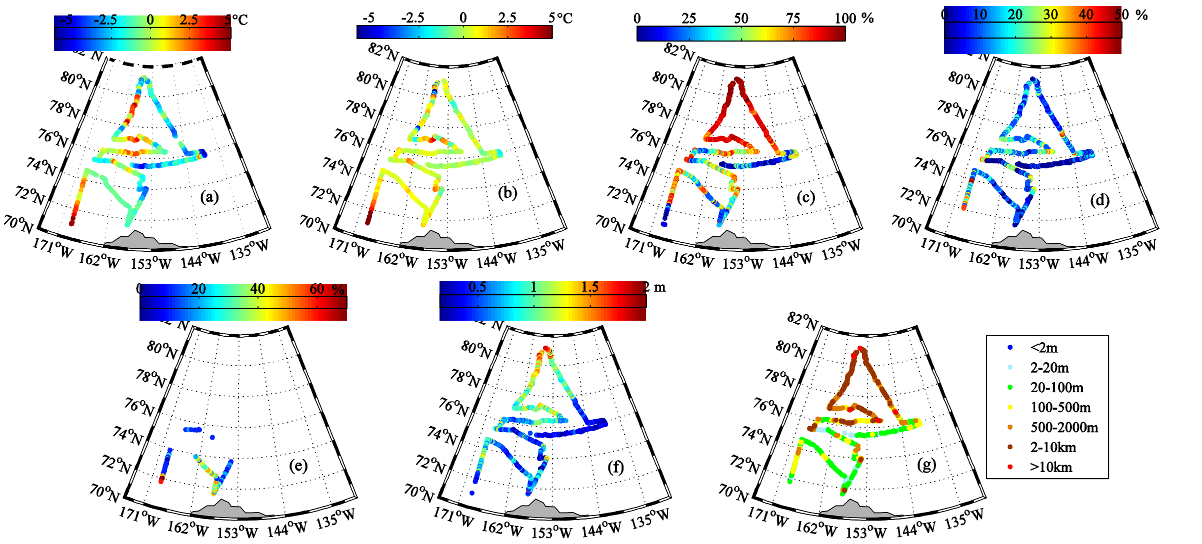

Fig. 5 Spatial distributions of surface air temperature measured by ship-based weather station (a) and surface temperature of ice/ocean measured by shipborne infrared radiation thermometer (b), sea ice concentration (c), melt pond and dirty ice fractions (d–e), sea ice thickness (f), and floe size (g) from visual observations.

Dirty impurity-laden ice was found only in the southwest of the study domain (Fig. 5e). The ice there may have grown in shallow near-coastal waters. During the ice growth season, waves and turbulence carry sediment from the seabed upward, where they may be trapped within the ice during freeze-up. Mammals on the sea ice may also trigger impurity transport to the ice surface. The drift of sea ice can transport the sediment further north and induce shelf-basin material exchange (Eicken et al., 2005). Impurities accumulated on or in sea ice are likely to affect the surface energy balance by lowering the overall albedo. Shipborne albedo measurements (data not shown here) revealed that the albedo of impurity-laden ice surface was 0.3–0.5, much smaller than snow-covered ice (0.6–0.8).

Floe diameters (Fig. 5g) were mostly > 2 km in the PIZ. In the MIZ, floe diameters were mostly < 500 m. The large floe size and ice concentration in the PIZ means that few leads formed.

3.2 Sea ice morphology at the long-term ice station

The freeboard data measured by borehole were interpolated to EM geolocations to estimate ice draft. The ice draft was 1.51±0.37 m and 1.31±0.06 m along P1 and P2, respectively (Fig. 6). Absolute deviations of ice draft were less than 0.10 m when compared with the borehole results. The largest deviation was in the transition area between level ice and ice ridges along P1, where ice draft from borehole and EM31 measurements was 1.49 m and 1.77 m, respectively. The main reason for this deviation was the poor lateral resolution of EM31 measurements. The EM31 footprint in the transition zone included both, level and ridged ice. In the measurement overlap part of P1, ice draft measured by the ULS was 1.42 ± 0.25 m and 1.42 ± 0.16 m during the frontward and backward navigations, respectively, comparable to the EM31 measurements (1.45 ± 0.12 m). However, along P2, EM31 and ULS measurements showed substantial deviations. We suspect that this was caused by the relatively large across transect change in ice draft. Consequently the offset in geolocations of surface and underwater measurements could produce some identifiable deviations. Compared with the EM31 measurements, the ULS measurements have two advantages. Firstly, the latter has a higher horizontal resolution, and secondly, it can sample a region that cannot be accessed from the surface. For example, in the melt-pond region of P1, the decrease of ice draft was measured by the ULS. This is because the lower albedo of melt pond allows more solar radiation to be absorbed, which results in the ice under a melt pond to melt more readily, generating a bottom depression that mirrors the pond on the top side (Wadhams et al., 2006).

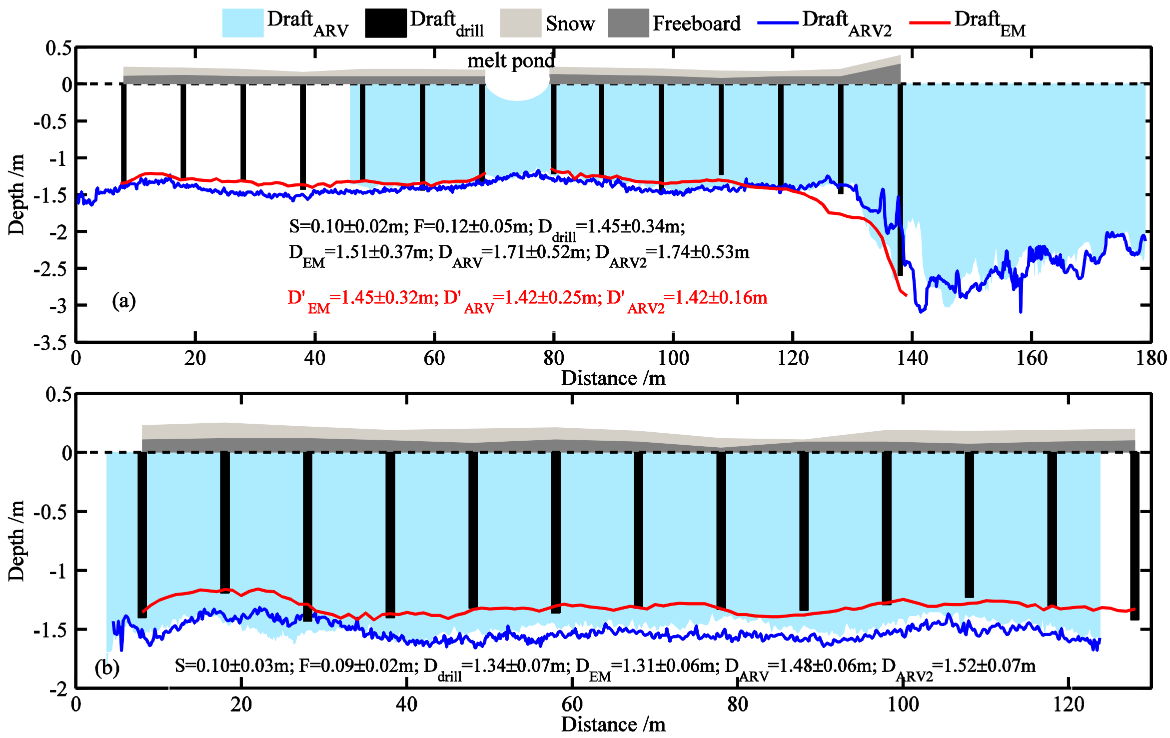

Fig. 6 Sea ice draft (D), freeboard (F) and snow depth (S) along the P1 and P2 measured by borehole, a ULS onboard the ARV and an EM31; blue area and curve show data from the ARV frontward and backward navigations. Average ± standard deviation: black for all data and red for overlap of EM31 and ARV measurements.

In Area 1, several melt ponds covered the lower right corner. Two ice ridges stretched from top to bottom at the left side and ~ 40–50 m from the right side (Fig. 2). These morphologic characteristics were identified by both the borehole and EM31 measurements on 19 August 2014 (Fig. 7). Data were two-dimensionally interpolated using kriging method (Oliver and Webster, 1990). Discrepancies between the data after and prior to the interpolation were less than 0.02m for both H_s and H_{s+i}, which demonstrates the applicability of the interpolation method. H_{s+i} measured by the EM31 (Fig. 7c) was in good agreement with the borehole measurements (Fig. 7a). The average bias was −0.03±0.11m, with 50% of the biases in the range −0.10 to 0.02 m. The EM31 data were mostly smaller than the borehole measurements at ice ridges and around melt ponds (Fig. 7d). As mentioned above, this can be explained by the low spatial resolution of EM31 measurements, which would be involved with some adjacent level ice for the measurement at ridges or ponded ice for the measurement around the pond. Snow depth in Area 1 was 0.03–0.15 m. Surfaces with substantial roughness, e.g., surrounding ridged ice, were likely covered by thicker snow, because snowdrifts are hampered over rough surfaces. A repeat EM31 measurement on 25 August 2014 yielded an average H_i of 1.35 m, very close to the average obtained on 19 August 2014 (1.37 m). This implies that the sea ice reached thermodynamic balance by that time. Lei et al. (2012b) showed that the melt rate of the ice bottom at latitude about 87°N was ~ 0.008 m per day from 9–18 August 2010. They argued that this can be attributed to the remarkable sea ice loss in the central Arctic Ocean during summer 2010, where numerous broad leads appeared among the floes, with an ice concentration of 70–85%. On the contrary, during the LS of CHINARE-2014, sea ice concentration was mainly > 95% in the study area. High ice concentration implies less solar radiation absorbed by the upper ocean and a weaker ocean-to-ice heat flux. This is likely the major reason for the near zero melt rate of the ice bottom during the LS of CHINARE-2014.

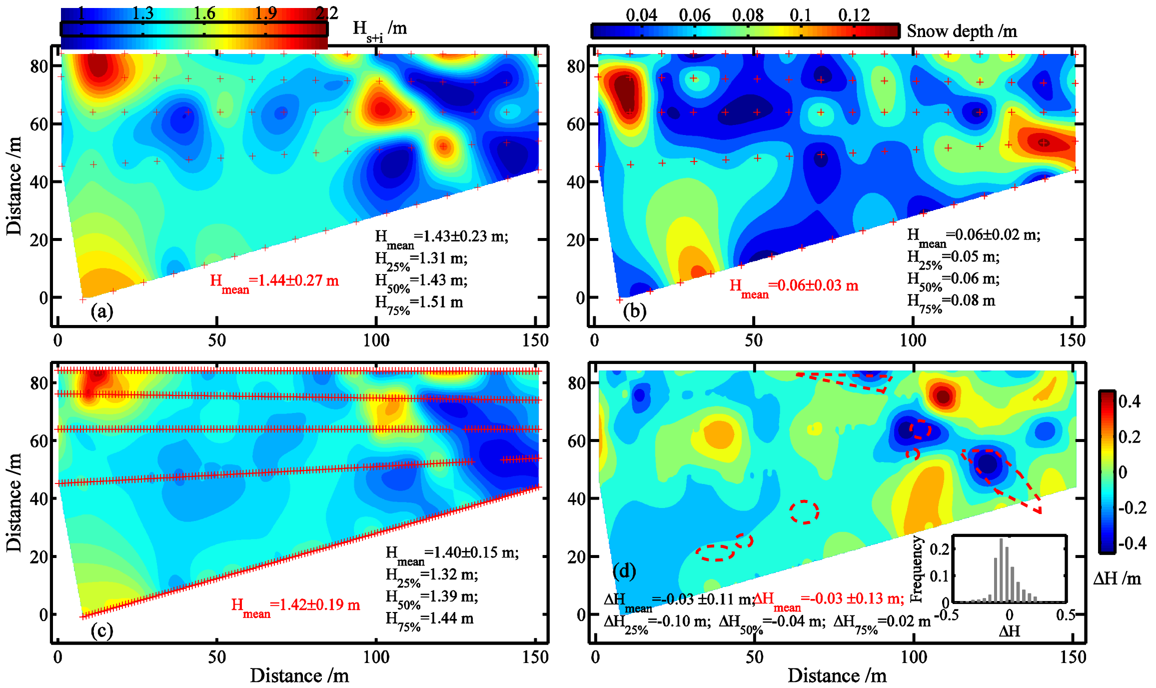

Fig. 7 Spatial distributions of H_{s+i} and H_s measured by borehole (a–b), H_{s+i} measured by EM31 on 19 August 2014 (c), and EM31 deviation from borehole measurements (d); inset shows corresponding frequency distributions. Red crosses denote measurement sites. Statistics for data prior to (red) and after (black) interpolation: H_{mean}, $H_{25\%}$, $H_{50\%}$, and $H_{75\%}$ indicate average, 25%, 50%, and 75% maxima of H_{s+i}, respectively. Dashed lines denote the rough outlines of melt ponds identified from surface as shown in Fig. 2.

The ice draft in Area 2 measured by the ULS onboard the ARV was also two-dimensionally interpolated using kriging method (Fig. 8). The absolute deviations of the average, 25%, 50% and 75% maxima of ice draft determined prior to and after the interpolation were < 0.05 m. Underwater measurements indicated substantial anisotropy of ice bottom morphology, and no linear ridge could be identified. A small hummock centered at −35 m and −15 m of the floe-referenced coordinate was observed in all underwater measurements. A relatively large melt pond centered near −63 m and −48 m (MP in Fig. 2). The ice draft under this melt pond was small (1.20–1.30 m). In general, low ice drafts (< 1.30

m) related to the surface melt pond. However, hummocks with ice draft of 2.0–2.9 m were nearly unidentifiable by surface visual observation, because of weathering. Based on all measurements data, the ice draft was 1.00–2.90 m. By adding snow depth and freeboard of 0.05–0.35 m, H_{s+i} was 1.05–3.25 m, which was in the range of the shipborne EM31 measurements (Fig. 3). From the comparisons between pair measurements of ARV, it is found that fifty percent of the deviations were less than ±0.20 m (Fig. 9). Although most deviations were relatively small, they had a wide distribution, ranging from −0.95 to 0.98 m. In contrast to the high along-track measurement resolution (0.10 m), the cross-track resolution was low, with a maximun of 10 m. In the overlap region, the ARV tracks had an offset between two launches, which could have caused ice draft deviations, especially in the region with large bottom roughness. Therefore, there are some limitations of using the DVL for the three-dimensional mapping of ice bottom morphology relative to a multibeam swath sonar (e.g., Wadhams et al., 2006; Williams et al., 2014).

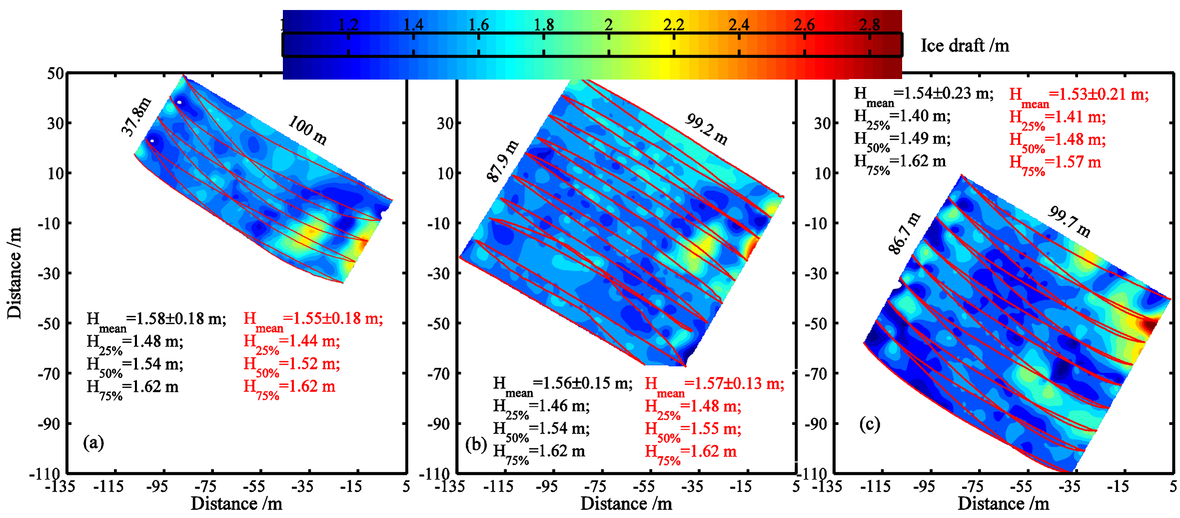

Fig. 8 Spatial distributions of sea ice draft measured by a ULS onboard the ARV at 0400 and 2100 on 21 August (a–b), and 0300 on 23 August 2014; red line is ARV track. Statistics, red and black for data prior to and after interpolation: H_{mean}, $H_{25\%}$, $H_{50\%}$, and $H_{75\%}$ denote average, 25%, 50%, and 75% maxima of ice draft, respectively.

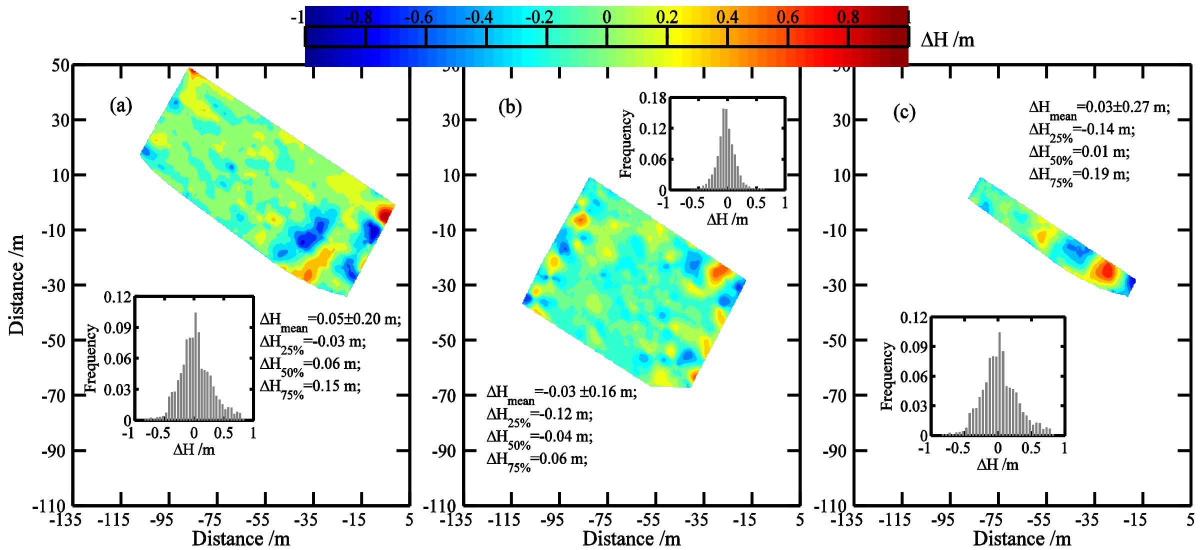

Fig. 9 Deviations of sea ice draft between data shown in Fig. 8b and 8a (a), between Fig. 8c and 8b (b) , and between Fig. 8c and 8a (c). Insets show corresponding frequency distributions. Statistical values are also shown.

3.3 Comparison with historic shipborne observations

Comparisons with historic shipborne observations showed that ice observed during the AOS94 experiment was the most compact (Fig. 10), because summer Arctic sea ice decreased remarkably during the succeeding two decades. In late July 1994, the southern boundaries of the MIZ and PIZ were around 69.9°N and 72.2°N. North of 72.2°N, sea ice concentration was generally > 85%. The sea ice was quite compact in both years 2003 and 2014. In these summers, boundaries of the PIZ were around 76–77°N in mid August, retreated northward < 100 km by early September, whereas the southern boundary of the MIZ retreated from ~ 71°N to ~ 75.5°N from late July to early September 2014, comparable with the years 2008 and 2010. Observations in 2008, 2010 and 2012 showed that even regions north of 83°N were covered by sea ice with concentration < 60%. In early September 2012, the MIZ was furthest north (~ 81°N), about 500–600 km further north than that in 2014, which agrees with the satellite-derived minimum Arctic sea ice extent during that summer.

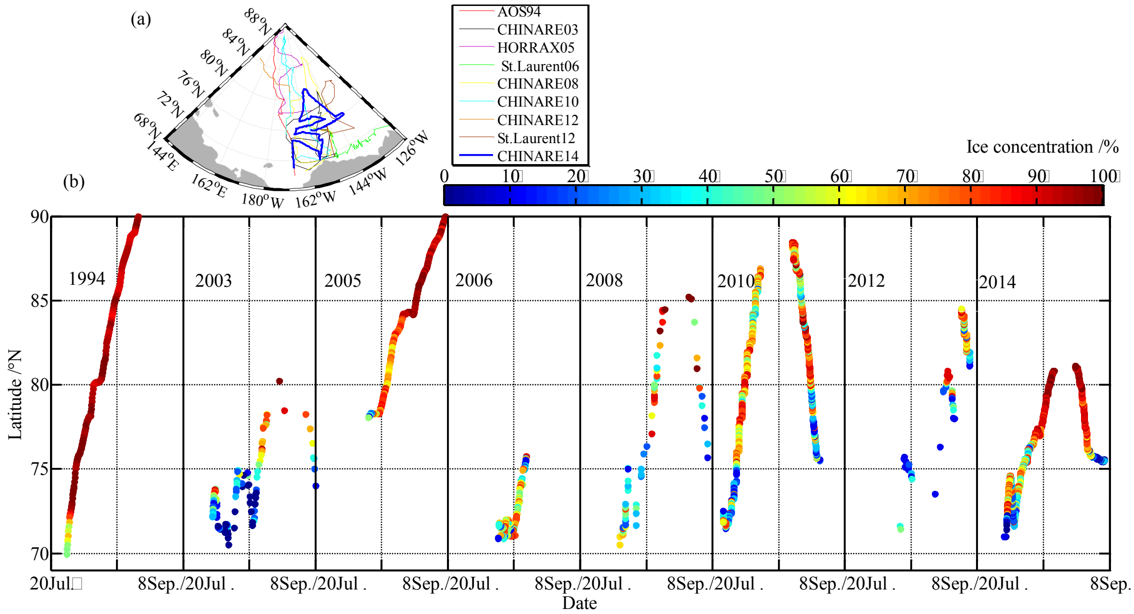

Fig. 10 (a) Trajectories of nine cruises from 1994 to 2014 in the Pacific section of Arctic Ocean; (b) sea ice concentration from shipborne observations.

To characterize changes in the ice volume, a local average sea ice thickness was defined as the ice thickness weighted by ice concentration. Similarly, to characterize changes in regional albedo, a local weighted average albedo could be obtained through visually observed sea ice concentration and melt pond fraction, and the assumed albedo for melt pond (0.3), sea ice (0.7), and open water (0.1), respectively. By late July to early August in 72°–76°N, the weighted average ice thickness and albedo obtained in 2014 were 0.37 m thicker and 0.1 larger than those in 2010 (Fig. 11). In 76–80.5°N, the weighted average ice thickness obtained in early-to-mid August 2014 was 0.54 m thicker than that for the same days of 2010, which implied a remarkable increase in sea ice volume in 2014. Accordingly, the weighted average albedo in 76–80.5°N obtained in 2014 was 0.1 larger than that in 2010. During CHINARE-2010, average albedo in late August for this region was much smaller than that observed 23–

28 days ago (0.31 vs. 0.47) due to the loss of sea ice cover. However, in late August 2014 this albedo increased slightly compared to that observed 10–20 days ago (0.58 vs. 0.57) due to the retention of sea ice concentration and surface refreezing. Consequently, about 27% less solar radiation could be absorbed by the ice-ocean system in late August for 2014 relative to 2010 in 76–80.5°N, assuming no change occured for the incident solar rdiation.

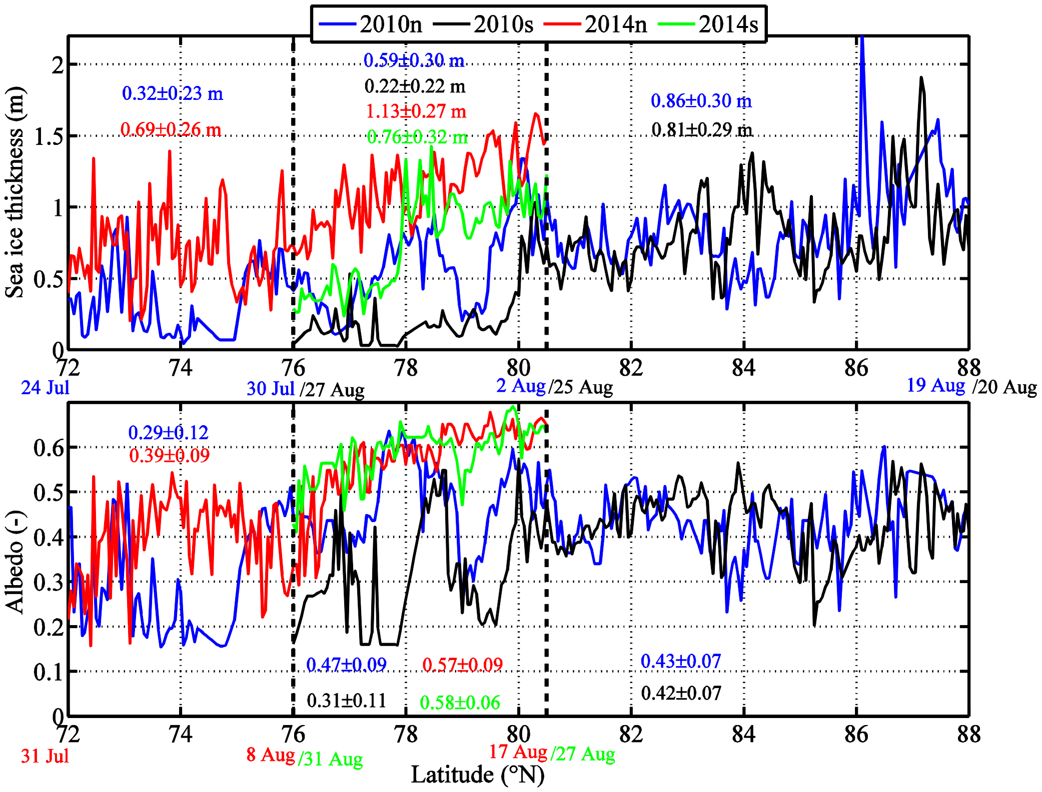

Fig. 11 Weighted average sea ice thickness (a) and surface albedo (b) along the northward and southward legs derived from shipborne visual observations during CHINARE-2010 and 2014. Also shown are the averages in the sub regions of 72–76°N, 76–80.5°N and 80.5–88°N.

3.4 Sea ice area and type determined from remotely sensed data

Although sea ice extent reached to the southern boundary of the defined domain on 29 July for all years 2003–2014, the spatial distribution of ice concentration on that day shows large interannual variability. The average sea ice area from 29 July to 6 September for the study years was 6.3×10^5 km^2. Prior to 2007, the sea ice area was relatively extensive (Fig. 12a), but after this year, the area clearly decreased, with some recoveries in 2009, 2013, and

2014. Seasonally, sea ice area reduced nearly linearly from 29 July to 6 September in all study years, with average reduction rate of 10.1×10^3 km^2 per day.

From Pearson correlation analysis, we found that the average sea ice area in the domain from 29 July to 6 September depended more strongly on the initial value on 29 July (R=0.91, P<0.001) than on the reduction rate through the sudy period (R=0.61, P<0.05). The average sea ice area in the study period correlated significantly with the average position of the southern boundaries of MIZ and PIZ (P<0.001). The relatively low initial value on 29 July (7.1×10^5 km^2) and the relatively high reduction rate until 6 September (15.5×10^3 km^2 per day) resulted in the smallest sea ice area in 2012 (2.6×10^5 km^2). In contrast, the initial values in 2013 and 2014 were relatively large (9.4×10^5 and 9.2×10^5 km^2), while the daily reduction rates until 6 September were relatively small and quasi-neutral, respectively (3.9×10^3 and 11.2×10^3 km^2 per day). Consequently, the average sea ice area in the study domain for these two years were relatively large. The average ice area during the 2014 study period was 7.6×10^5 km^2, which was the fourth among 2003–2014, and second since 2007 (Fig. 12b). During 2003–2014, interannual variability of ice area in the domain was consistent with that of average Arctic-wide sea ice extent and of annual minimum Arctic sea ice extent (Fig. 12b). The first can explain the latter two by 53.2% (P<0.05) and 65.5% (P<0.01), respectively. This implies that the interannual variability of summer sea ice in the domain is very vital for the entire Arctic Ocean.

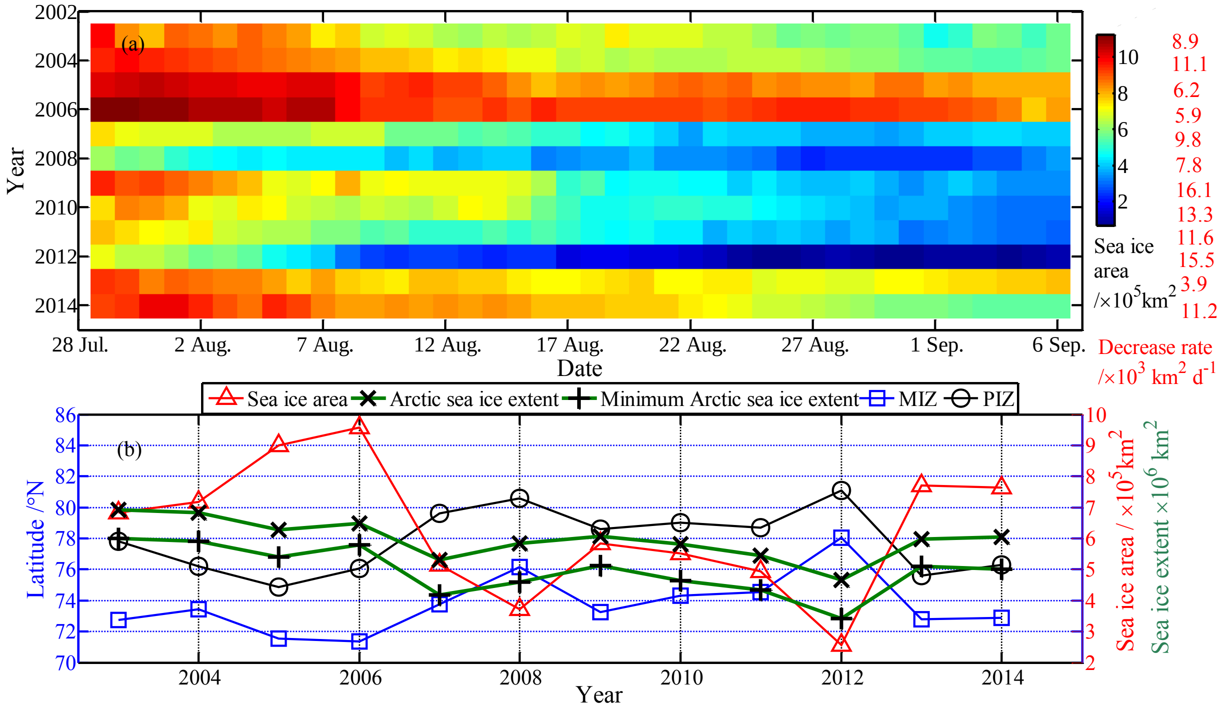

Fig. 12 (a) Changes in daily sea ice area derived from AMSR-E/AMSR2 data in the study domain from 29 July through 6 September in years 2003–2014; also shown is the decreased rate from 29 July to 6 September for each year. (b) Interannual changes in sea ice area and southern boundaries of MIZ and PIZ in the study domain and sea ice extent in entire Arctic Ocean averaged over 29 July–6 September, and annual minimum Arctic sea ice extent from 2003 to 2014.

Although the study domain was almost completely covered by sea ice on 30 April during the years 2005–2014, the ratio between first-year ice and multiyear ice showed strong interannual variability (Fig. 13). The decrease of multiyear ice area in the study domain was remarkable in the years after 2006. Noteworthy was a substantial recovery in 2014, to an amount of 7.8×10^5 km^2, which was larger than that in 2006 (7.4×10^5 km^2). Sea ice drift in the domain is mostly driven by the clockwise Beaufort Gyre (Kwok et al., 2013). From the ITP GPS data (Fig. 13a) we found that, in the southeast region of our defined domain, the inflow sea ice was advected from north of the Canadian Arctic Archipelago from 30 April to 6

September 2014, which was mostly multiyear ice. In contrast, first-year ice in the southwest of our domain moved into the western Chukchi Sea. In the northwest of the domain, sea ice drifted northward. Consequently, first-year and multiyear ice in the region are redistributed. Furthermore, the Beaufort Gyre would supply mostly multiyear ice from the north into the northeast of the domain. From a kinematic view, the fraction of multiyear ice within our domain would increase from 30 April to 6 September 2014, which means that, relatively large fraction of multiyear ice observed on 30 April 2014 would retain through the summer.

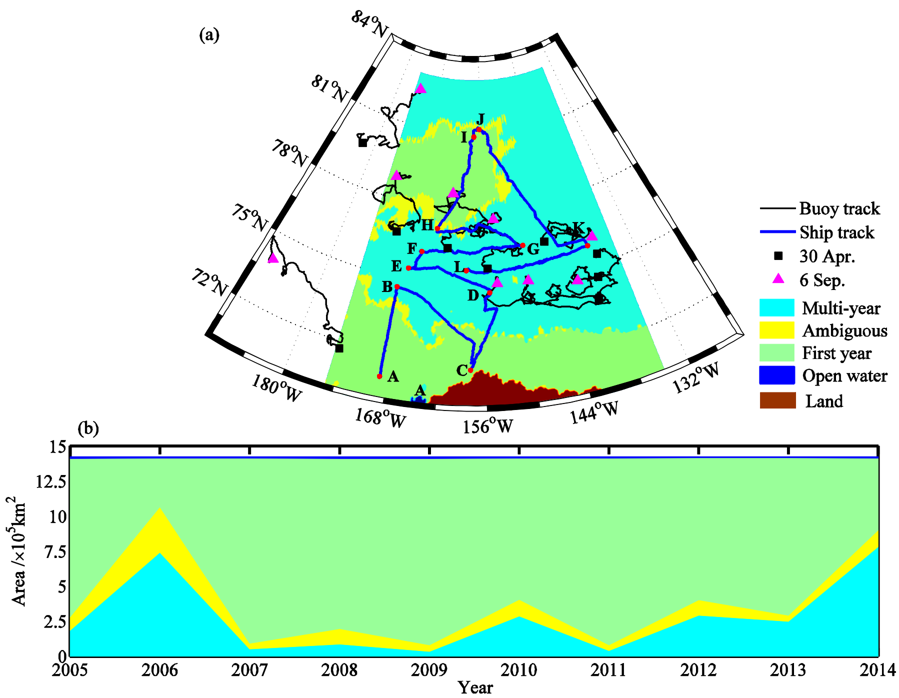

Fig. 13 (a) Sea ice classification in the defined domain on 30 April 2014 obtained from the OSI-SAF dataset, trajectory of the *Xuelong* (blue), and ITP trajectories (black) from 30 April to 6 September 2014; (b) interannual changes in sea ice areas of various classifications on 30 April, 2005–2014.

4 Discussions

From 2005 to 2014, a composite of AO and DA from September through February could explain the fraction of multiyear ice in the study domain on 30 April by 72% (R^2; Fig. 14a). Both negative AO and DA from September through February were closely related to the large coverage of multiyear ice on 30 April. This could be explained by enhanced inflow advection from north of the Canadian Arctic Archipelago, owing to anticyclonic wind anomalies and reduced outflow advection into the Trans-polar Drift Stream (TDS) caused by anomalous south meridional winds in the study domain under the negative AO and DA (Kwok et al., 2013; Wang et al., 2009). In the years 2003–2014, combination of yearly AO and DA indices could explain average sea ice coverage from 29 July through 6 September in the study domain by 44% (R^2; Fig. 14b). However, the contribution of AO in this regression was negligible. Removing the AO, the yearly DA alone could explain 52% of the variability in the summer ice cover (Fig. 14c). This emphasizes the importance of DA to the summer sea ice condition in the study domain.

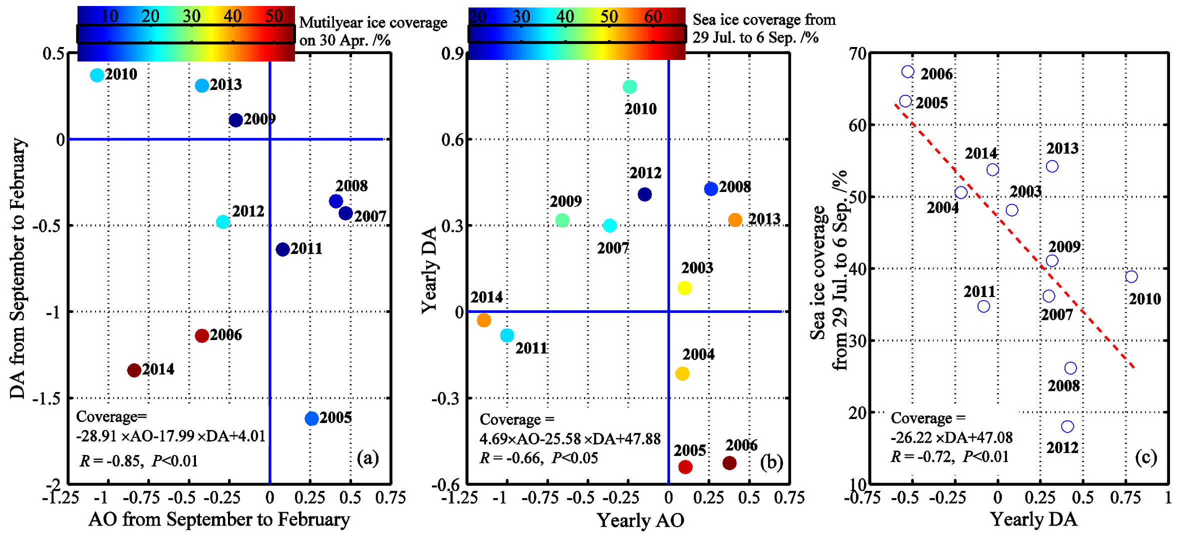

Fig. 14 (a) Relationships between coverage of multiyear sea ice in the study domain on 30 April and the DA/AO indices from September through February; (b) between average sea ice coverage in the study domain over 29 July–6 September and yearly DA/AO indices, and (c) between average sea ice coverage in the study domain over 29 July–6 September and yearly DA index.

The average AO and DA indices were −0.84 and −1.34 from September 2013 through February 2014, much lower than their averages between 2002 and 2014 (−0.16 and −0.40, respectively). This implies strong sea ice inflow from north of the Canadian Arctic Archipelago and weak outflow into the TDS between September 2013 and February 2014. Therefore, the multiyear ice concentration in the study domain on 30 April was greatest in 2014 (55%) among 2005–2014. From March–August 2014, the AO index remained extremely low (−1.28) and DA was relatively high (1.28), compared with their averages for 2002–2014 (−0.16 and 0.61). This suggests strong inflow through the eastern boundary and strong outflow through the northern boundaries of the study domain from March–August 2014, as shown in Fig. 13a. There was a relatively rapid retreat of the MIZ from late July through early September 2014, which was associated with invigorated south winds under the positive DA. However, the enhanced south winds were unable to produce abundant open waters in the PIZ during summer 2014, because of the large fraction of compact and thick multiyear ice.

Kwok (2015) found that an outstanding sea ice convergence occurred along the coast of Canadian Arctic Archipelao during the summer of 2013, due to a strong wind-driven onshore ice drift. This resulted in an sea ice area compressing by 23% and an increase in ice thickness by ~30% for this region. Under the strongly negative polarity of the AO from September 2013 through August 2014 (−1.14), the deformed ice along the coast of Canadian Arctic Archipelao was likely to be advected into our study domain. Therefore, the relatively deformed and compact sea ice observed during the CHINARE-2014 was mainly caused by year-round negative polarity of the AO.

5 Conclusions

Both, the remotely sensed passive microwave as well as shipborne observations indicated that summer 2014 exhibited highly compact and deformed sea ice. This may be attributed to a number of factors, including a remarkable sea ice convergence occuring along the coast of Canadian Arctic Archipelao during the summer of 2013, an AO with strong negative polarity during September 2013–August 2014, promoting multiyear sea ice inflow from north of the Canadian Arctic Archipelago into the sector, and a DA with strong negative polarity during September 2013–February 2014, which was responsible for a weakened sea ice outflow from the study domain into the TDS. In contrast, the strong positive polarity of DA during March–August 2014 resulted in a strong south wind and rapid retreat of the MIZ in the study sector during the summer. However, due to the large concentration of multiyear sea ice, the PIZ showed persistence from late July to early September 2014, which was manifested by a little retreat of the PIZ boundary (< 100 km), persistent high ice concentration and large floe size, and no extensive open water in that region.

By late July, shipborne observations during CHINARE-2014 showed that, the sea ice in the MIZ from 71.0° to 76.2°N was mostly deformed becuse thin level ice had aready melted, resulting in poor agreement between ice thickness data from visual observations and EM measurements. Upon entering the PIZ, the contribution of ice ridges to the ice thickness distribution decreased with increase of level ice. Level ice thickness increased from 0.4–1.4 m near 76°N to 1.1–2.0 m near 81°N. Observations along the southward track from 26 August through 6 September differed from those along southward track from 29 July through 17 August in diverse aspects: Firstly, surface refreezing occurred along southward track, accompanied by reduced surface temperature and increased surface albedo. Secondly, ice thickness decreased remarkably in the southern PIZ, which could be attributed to the substantial oceanic heat from the MIZ. Thirdly, the southern boundary of the MIZ has retreated by about 450–550 km along southward track.

From underwater ULS measurements, we found that basal topography under melt ponds mirrored the top surface structure due to local albedo feedback. However, not all ice hummocks or ridges observed by the ULS can be identified by surface observation due to weathering. Compared with the shipborne and ground-based EM measurements, the ULS onboard the ARV provided high-resolution three-dimensional measurements, which is nontrivial because of the strong anisotropy of ice bottom morphology. For the ULS measurements, cross-track resolution needs also to be considered, especially for regions with strong spatial change in ice draft.

At the LS at 81°N, the mode of H_{s+i} from the ground-based EM was 1.48 m. No significant sea ice melt was observed during the LS in late August 2014. This was clearly different from the conditions during 2010 summer, when substantial open water appeared in the central Arctic Ocean and sea ice melt was still identifiable at ~ 87°N (Lei et al., 2012b). Larger multiyear ice inflow during the winter, less sea ice melt in the subsequent summer, and earlier sea ice refreezing in the fall were likely to constitutes a feedback loop from 2013 to 2014.

Acknowledgements

This work was financially supported by the National Natural Science Foundation of China (No. 41476170) and Chinese Polar Environment Comprehensive Investigation and Assessment Programs (Nos. CHINARE2015-03-01/04-03/04-04). JW was supported by the NOAA CPO Office of Arctic Research through RUSALCA project, which was GLERL Contribution (No. 1821). PH was supported by the Antarctic Climate and Ecosystems CRC program. This work contributs to Australian Antarctic Science project (No. 4301).

References

Comiso, J. C., 2012: Large decadal decline of the Arctic multiyear ice cover, *J. Clim.*, 25, 1176–1193. doi: http://dx.doi.org/10.1175/JCLI-D-11-00113.1.

Eastwood, S., 2012: OSI-SAF sea ice product manual, v3.8. EUMETSAT. Satellite Application Facility on Ocean and Sea Ice, available at http://osisaf.met.no/p/ice/.

Eicken, H., Gradinger, R., Gaylord, A., Mahoney, A., Rigor, I., and Melling, H., 2005: Sediment transport by sea ice in the Chukchi and Beaufort Seas: Increasing importance due to changing ice conditions? *Deep-Sea Res. II*, 52, 3281–3302.

Fetterer, F., Knowles, K., Meier, W., and Savoie, M., (2002): Updated daily. Daily sea ice index, Boulder, Colorado, USA, National Snow and Ice Data Center, 2002.

Haas, C., 1998: Evaluation of ship-based electromagnetic-inductive thickness measurements of summer sea-ice in the Bellingshausen and Amundsen Seas, Antarctica. *Cold Reg*. *Sci*. *Technol*. 27, 1–16.

Kistler, R., et al., 2001: The NCEP-NCAR 50-year reanalysis: Monthly means CD-ROM and documentation, *Bull*. *Am*. *Meteorol*. *Soc*., 82, 247–268.

Kovacs, A., Holladay, J. S., and Bergeron, C. J. 1995: The footprint/altitude ratio for helicopter electromagnetic sounding of sea-ice thickness: Comparison of theoretical and field estimates, *Geophysics*, 60, 374–380.

Kwok, R., and Cunningham, G. F., 2010: Contribution of melt in the Beaufort Sea to the decline in Arctic multiyear sea ice coverage: 1993–2009, *Geophys*. *Res*. *Lett*., 37, L20501, doi:10.1029/2010GL044678.

Kwok, R., and Rothrock, D. A., 2009: Decline in Arctic sea ice thickness from submarine and ICESat records: 1958-2008, *Geophys*. *Res*. *Lett*., 36, doi:10.1029/2009GL039035.

Kwok, R., Spreen, G., and Pang, S., 2013: Arctic sea ice circulation and drift speed: Decadal trends and ocean currents, *J*. *Geophys*. *Res*., 118, 2408–2425, doi:10.1002/jgrc.20191.

Kwok, R., 2015: Sea ice convergence along the Arctic coasts of Greenland and the Canadian Arctic Archipelago: Variability and extremes (1992–2014). *Geophysical Research Letters*, doi:10.1002/2015GL065462.

Laxon, S. W., Giles, K. A., Ridout, A. L., Wingham, D. J., Willatt, R., Cullen, R., Kwok, R., Schweiger, A., Zhang, J., Haas, C., Hendricks, S., Krishfield, R., Kurtz, N., Farrell, S., and Davidson, M., 2013: CryoSat-2 estimates of Arctic sea ice thickness and volume, *Geophys*. *Res*. *Lett*. 40, 732–737, doi:10.1002/grl.50193.

Lei, R., Li, Z., Li, N., Lu, P., and Cheng, B., 2012a: Crucial physical characteristics of sea ice in the Arctic section of 143°W-180°W during August and early September 2008, *Acta Oceanol*. *Sin*., 31(4), 65–75.

Lei, R., Zhang, Z., Matero, I., Cheng, B., Li, Q., and Huang, W., 2012b: Reflection and transmission of irradiance by snow and sea ice in the central Arctic Ocean in summer 2010. *Polar Res*., 31, 17325, doi: 10.3402/polar.v31i0.17325.

Lei, R., Tian-Kunze, X., Leppäranta, M., Wang, J., Kaleschke, L., and Zhang, Z., 2016: Changes in summer sea ice, albedo, and portioning of surface solar radiation in the Pacific sector of Arctic Ocean during 1982–2009, *J. Geophys. Res.*, 121, 5470–5486, doi:10.1002/2016JC011831.

Li, Z., Zhang, Z., Lu, P., Dong, X., Cheng, B., and Chen, Z., 2005: Some parameters on Arctic sea ice dynamics from the expedition in the summer of 2003. *Acta Oceanol*. *Sin*., 24, 6, 54–61.

Lu, P., Li, Z., Cheng, B., Lei, R., and Zhang, R., 2010: Sea ice surface features in Arctic summer 2008: Aerial observations, *Remote Sens*. *Environ*., 114, 693–699, doi:10.1016/j.rse.2009.11.009.

Lu, P., Li, Z, Cheng, B., and Leppäranta, M., 2011: A parameterization of the ice-ocean drag coefficient, *J*. *Geophys*. *Res*., 116, C07019, doi:10.1029/2010JC006878, 2011.

Oliver, M. A., and Webster, R., 1990: Kriging: A method of interpolation for geographical information system, *Int*. *J*. *Geogr*. *Inf*. *Sys*., 4, 3, 313–332.

Perovich, D. K., Richter-Menge, J. A., Jones, K. F., and Light, B., 2008: Sunlight, water, and ice: Extreme Arctic sea ice melt during the summer of 2007, *Geophys*. *Res*. *Lett*., 35, L11501, doi:10.1029/2008GL034007.

Perovich, D. K., Grenfell, T. C., Light, B., Elder, B. C., Harbeck, J., Polashenski, C., Tucker III, W. B., and Stelmach, C., 2009: Transpolar observations of the morphological properties of Arctic sea ice, *J*. *Geophys*. *Res*., 114, C00A04, doi:10.1029/2008JC004892.

Shimada, K., Kamoshida, T., Itoh, M., Nishino, S., Carmack, E., McLaughlin, F. A., Zimmermann, S., and Proshutinsky, A., 2006: Pacific Ocean inflow: Influence on catastrophic reduction of sea ice cover in the Arctic Ocean, *Geophys*. *Res*. *Lett*., 33, L08605, doi:10.1029/2005GL025624.

Spreen, G., Kaleschke, L., and Heygster G., 2008: Sea ice remote sensing using AMSR-E 89 GHz channels, *J*. *Geophys*. *Res*., 113, C02S03, doi:10.1029/2005JC003384.

Tin, T., and Jeffries, M., 2003: Morphology of deformed first-year sea ice features in the Southern Ocean, *Cold Reg*. *Sci*. *Techno*., 36, 141–163.

Tucker III, W. B., Gow, A. J., Meese, D. A., Bosworth, H. W., and Reimnitz, E., 1999: Physical characteristics of summer sea ice across the Arctic Ocean, *J*. *Geophys*. *Res*., 104(C1): 1489–1504, doi:10.1029/98JC02607.

Wadhams, P., Wilkinson, J. P., and McPhail, S. D., 2006: A new view of the underside of Arctic sea ice, *Geophys*. *Res*. *Lett*., 33, L04501, doi:10.1029/ 2005GL025131.

Wang, J., Zhang, J., Watanabe, E., Mizobata, K., Ikeda, M., Walsh, J. E., Bai, X., and Wu, B., 2009: Is the Dipole Anomaly a major driver to record lows in the Arctic sea ice extent? *Geophys*. *Res*. *Lett*. 36, L05706, doi:10.1029/2008GL036706.

Wei, J., and Su, J., 2014: Mechanism of an abrupt decrease in sea-ice cover in the Pacific Sector of the Arctic during the late 1980s, *Atmos*. *Ocean*, 52(5), 434-445.

Williams, G., Maksym, T., Wilkinson, J., Kunz, C., Murphy, C., Kimball, P., and Singh, H., 2014: Thick and deformed Antarctic sea ice mapped with Autonomous Underwater Vehicles, *Nat*. *Geosci*., doi:doi:10.1038/NGEO2299.

Worby, A. P., and Allison, I., 1999: A technique for making ship-based observations of Antarctic sea ice thickness and characteristics, Part 1: Observational techniques and results, Antarctic CRC Research Report, 14, ISBN: 1875796096, Hobart, Tasmania, Australia, 23pp.

Wu, B., Wang, J., Walsh, J. E., 2006: Dipole Anomaly in the winter Arctic atmosphere and its association with Arctic sea ice motion, *J*. *Clim*. 19, 210– 225, doi:10.1175/JCLI3619.1.

Xia, W., Xie, H, and Ke, C., 2014: Assessing trend and variation of Arctic sea ice extent during 1979-2012 from a latitude perspective of ice edge, Polar *Res*., 33, 21249, doi: 10.3402/polar.v33.21249.

Xie, H., Lei, R., Ke, C., Wang, H., Li, Z., Zhao, J., and Ackley, S. F., 2013: Summer sea ice characteristics and morphology in the Pacific Arctic sector as observed during the CHINARE 2010 cruise, *Cryosphere*, 7(4), 1057–1072.

Highlights

- **Summer Arctic sea ice morphology has been measured using multi-scale methods**
- **The PSA had compact sea ice in summer 2014 due to year-round negative AO**
- **Larger winter ice inflow and less summer melt induced earlier refreezing in 2014**

Fig.1

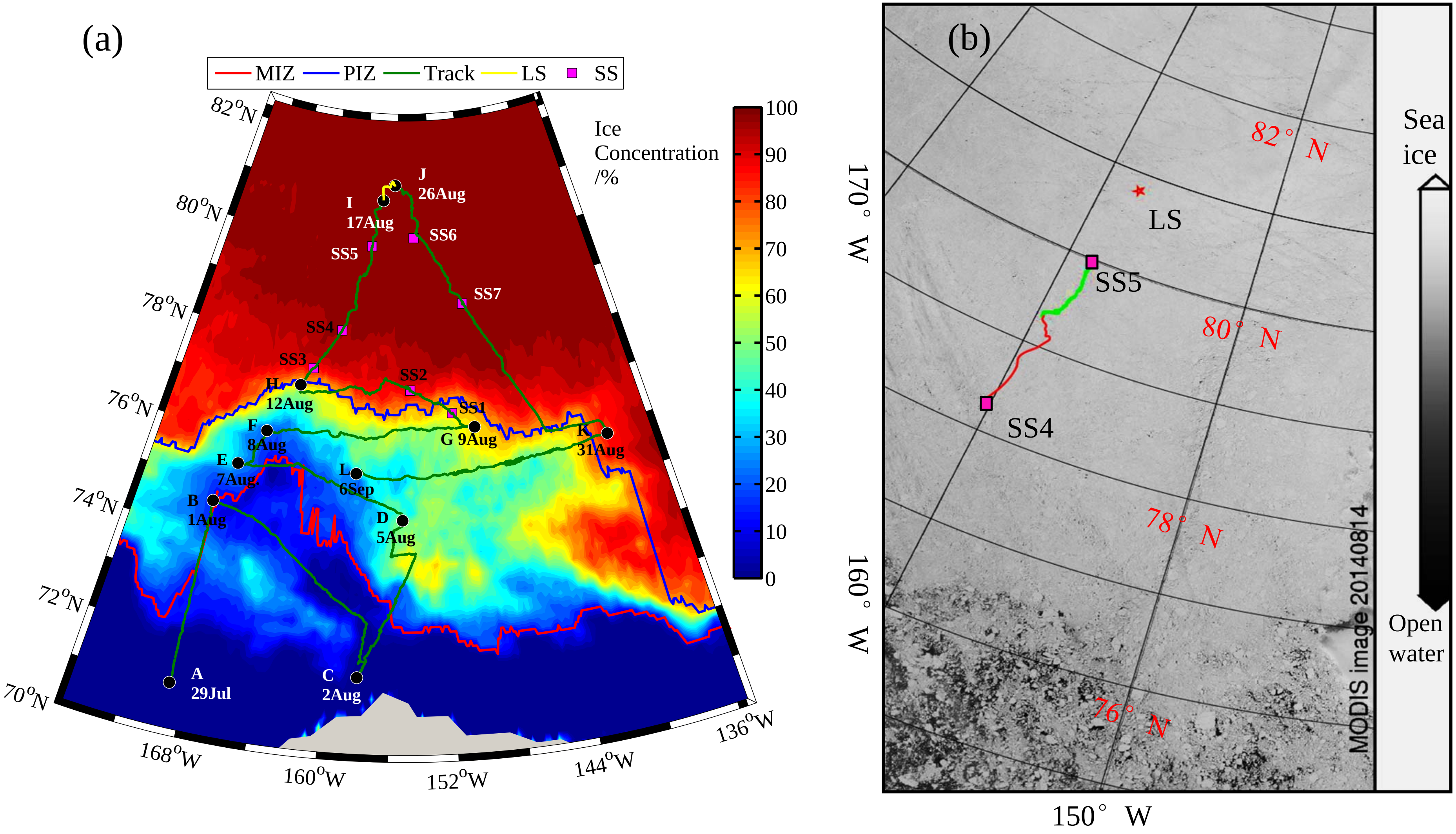
(a)
MIZ
PIZ
Track
LS
SS
Ice Concentration /%
100
90
80
70
60
50
40
30
20
10
0
82°N
80°N
78°N
76°N
74°N
72°N
70°N
168°W
160°W
152°W
144°W
136°W
A 29Jul
B 1Aug
C 2Aug
D 5Aug
E 7Aug
F 8Aug
G 9Aug
H 12Aug
I 17Aug
J 26Aug
K 31Aug
L 6Sep
SS1
SS2
SS3
SS4
SS5
SS6
SS7
(b)
170° W
160° W
150° W
82° N
80° N
78° N
76° N
LS
SS5
SS4
MODIS image 20140814
Sea ice
Open water

Fig.2

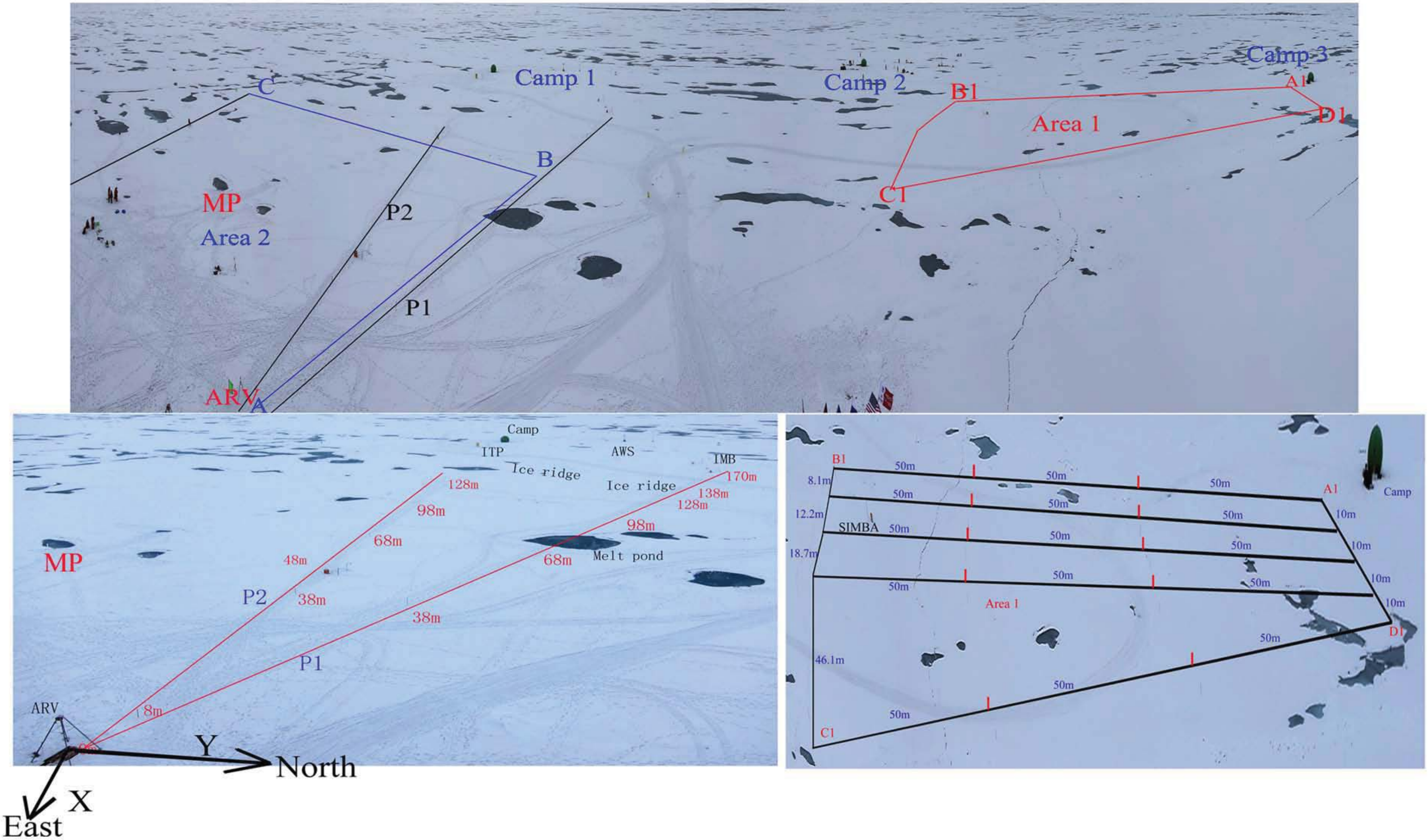
Camp 1
Camp 2
Camp 3
C
B
A
P2
P1
MP
Area 2
ARV
B1
A1
D1
C1
Area 1
Camp
ITP
AWS
IMB
Ice ridge
Ice ridge
Melt pond
128m
98m
68m
48m
38m
8m
170m
138m
128m
98m
68m
38m
MP
P2
P1
ARV
Y
North
X
East
B1
50m
50m
50m
A1
Camp
8.1m
12.2m
18.7m
46.1m
10m
10m
10m
10m
SIMBA
50m
50m
50m
50m
50m
50m
50m
50m
50m
Area 1
D1
50m
50m
50m
C1

Fig.3

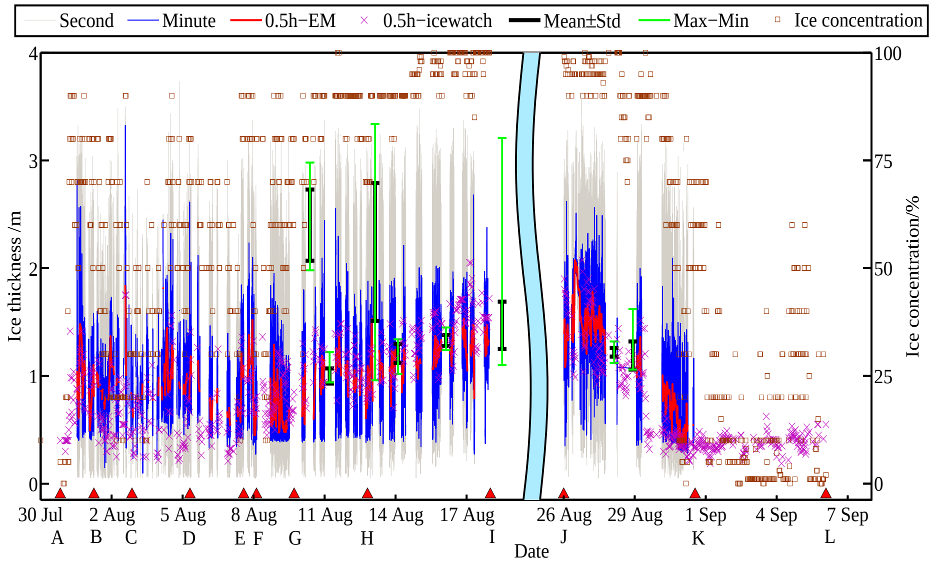
Second
Minute
0.5h−EM
0.5h−icewatch
Mean±Std
Max−Min
Ice concentration
Ice thickness /m
Ice concentration/%
Date
30 Jul
2 Aug
5 Aug
8 Aug
11 Aug
14 Aug
17 Aug
26 Aug
29 Aug
1 Sep
4 Sep
7 Sep
A
B
C
D
E
F
G
H
I
J
K
L

Figure(s)

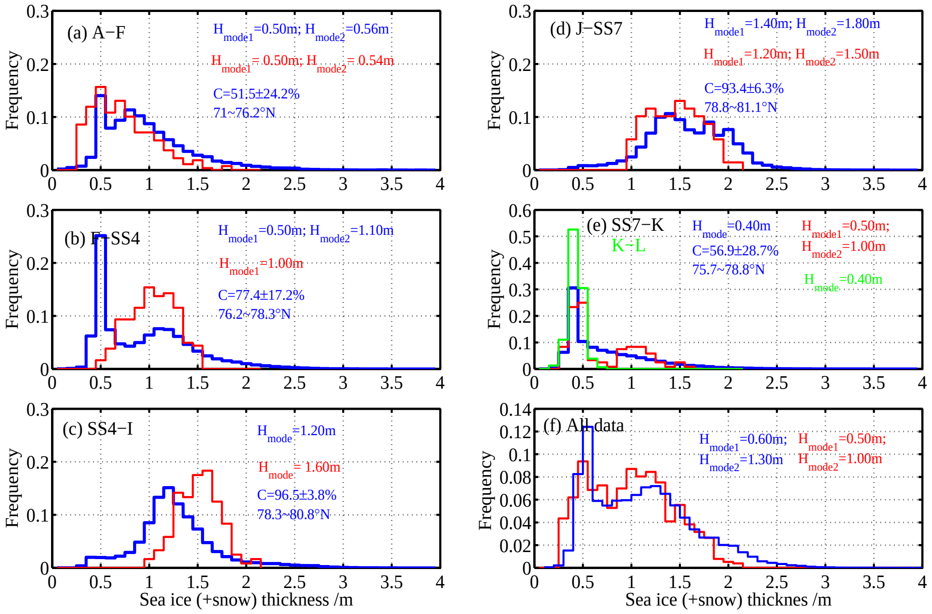

(a) A−F
H mode1 =0.50m; H mode2 =0.56m
H mode1 = 0.50m; H mode2 = 0.54m
C=51.5±24.2%
71~76.2°N
(b) F−SS4
H mode1 =0.50m; H mode2 =1.10m
H mode1 =1.00m
C=77.4±17.2%
76.2~78.3°N
(c) SS4−I
H mode =1.20m
H mode = 1.60m
C=96.5±3.8%
78.3~80.8°N
(d) J−SS7
H mode1 =1.40m; H mode2 =1.80m
H mode1 =1.20m; H mode2 =1.50m
C=93.4±6.3%
78.8~81.1°N
(e) SS7−K
K−L
H mode =0.40m
C=56.9±28.7%
75.7~78.8°N
H mode1 =0.50m;
H mode2 =1.00m
H mode =0.40m
(f) All data
H mode1 =0.60m;
H mode2 =1.30m
H mode1 =0.50m;
H mode2 =1.00m
Frequency
Sea ice (+snow) thickness /m
Sea ice (+snow) thicknes /m

Fig.5

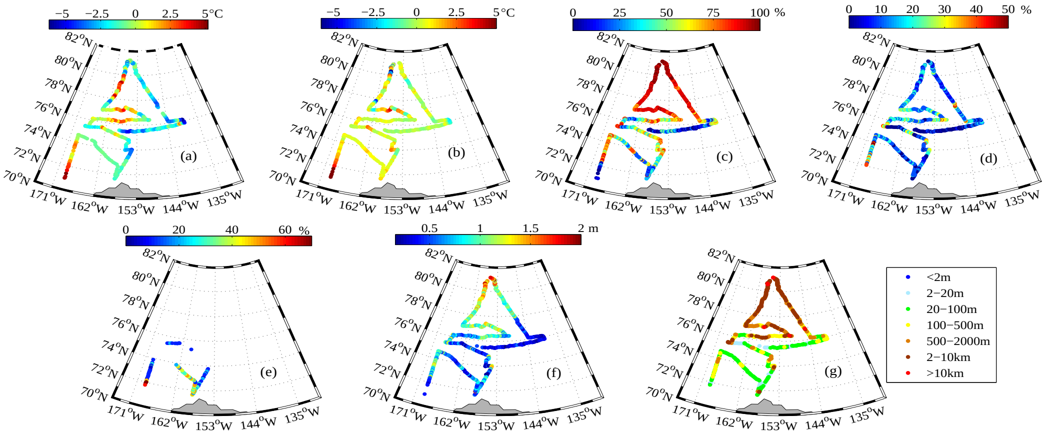

Fig.6

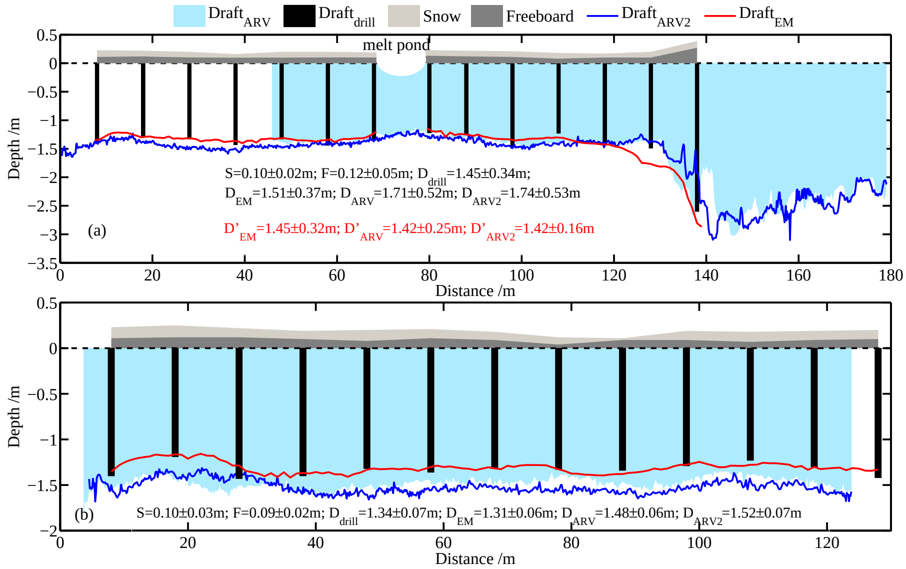
Draft ARV
Draft drill
Snow
Freeboard
Draft ARV2
Draft EM
melt pond
Depth /m
Distance /m
(a)
S=0.10±0.02m; F=0.12±0.05m; D drill=1.45±0.34m;
D EM=1.51±0.37m; D ARV=1.71±0.52m; D ARV2=1.74±0.53m
D' EM=1.45±0.32m; D' ARV=1.42±0.25m; D' ARV2=1.42±0.16m
(b)
S=0.10±0.03m; F=0.09±0.02m; D drill=1.34±0.07m; D EM=1.31±0.06m; D ARV=1.48±0.06m; D ARV2=1.52±0.07m

Figure(s)

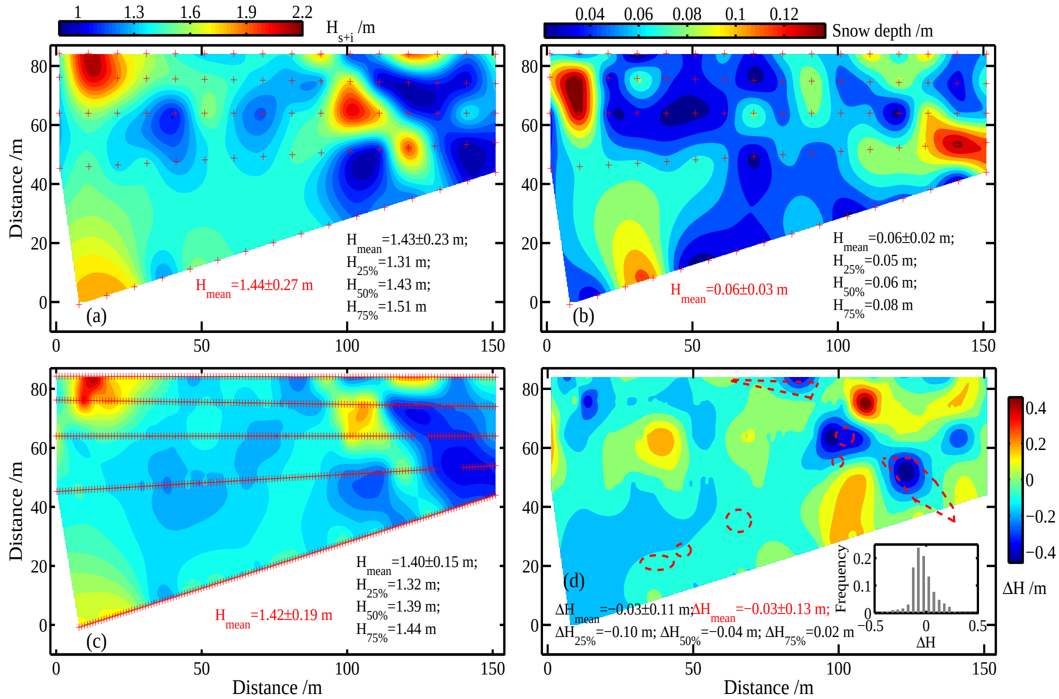

1 1.3 1.6 1.9 2.2
Hs+i /m
0.04 0.06 0.08 0.1 0.12
Snow depth /m
Distance /m
(a)
Hmean=1.43±0.23 m;
H25%=1.31 m;
H50%=1.43 m;
H75%=1.51 m
Hmean=1.44±0.27 m
(b)
Hmean=0.06±0.02 m;
H25%=0.05 m;
H50%=0.06 m;
H75%=0.08 m
Hmean=0.06±0.03 m
(c)
Hmean=1.40±0.15 m;
H25%=1.32 m;
H50%=1.39 m;
H75%=1.44 m
Hmean=1.42±0.19 m
(d)
ΔHmean=−0.03±0.11 m; ΔHmean=−0.03±0.13 m;
ΔH25%=−0.10 m; ΔH50%=−0.04 m; ΔH75%=0.02 m
Frequency
ΔH
ΔH /m

Fig.8

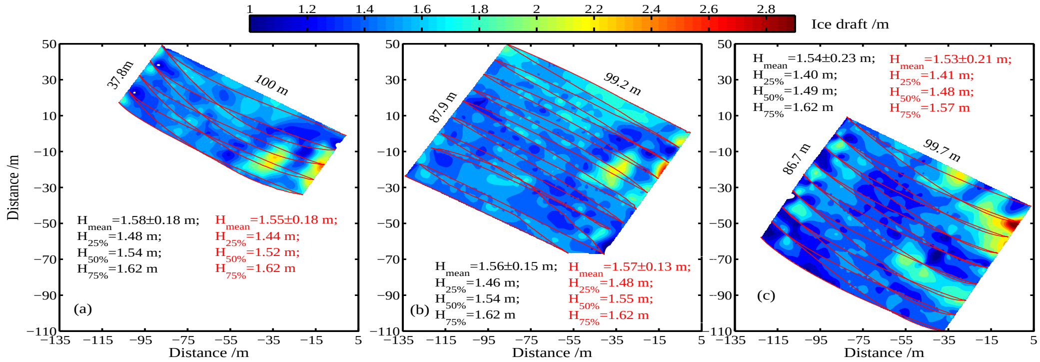

1
1.2
1.4
1.6
1.8
2
2.2
2.4
2.6
2.8
Ice draft /m
37.8m
100 m
Distance /m
H_mean=1.58±0.18 m;
H_25%=1.48 m;
H_50%=1.54 m;
H_75%=1.62 m
H_mean=1.55±0.18 m;
H_25%=1.44 m;
H_50%=1.52 m;
H_75%=1.62 m
(a)
Distance /m
87.9 m
99.2 m
H_mean=1.56±0.15 m;
H_25%=1.46 m;
H_50%=1.54 m;
H_75%=1.62 m
H_mean=1.57±0.13 m;
H_25%=1.48 m;
H_50%=1.55 m;
H_75%=1.62 m
(b)
Distance /m
H_mean=1.54±0.23 m;
H_25%=1.40 m;
H_50%=1.49 m;
H_75%=1.62 m
H_mean=1.53±0.21 m;
H_25%=1.41 m;
H_50%=1.48 m;
H_75%=1.57 m
86.7 m
99.7 m
(c)
Distance /m

Fig.9

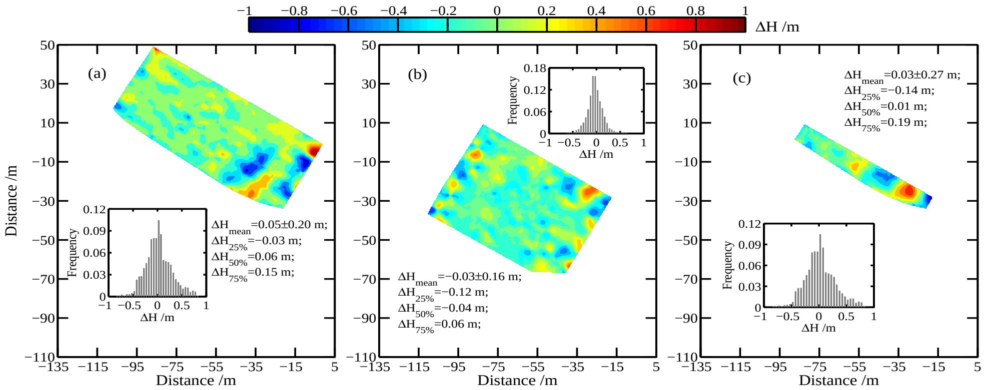

−1 −0.8 −0.6 −0.4 −0.2 0 0.2 0.4 0.6 0.8 1
ΔH /m
(a)
(b)
(c)
Distance /m
Distance /m
Frequency
ΔH /m
ΔH$_{mean}$=0.05±0.20 m;
ΔH$_{25\%}$=−0.03 m;
ΔH$_{50\%}$=0.06 m;
ΔH$_{75\%}$=0.15 m;
ΔH$_{mean}$=−0.03±0.16 m;
ΔH$_{25\%}$=−0.12 m;
ΔH$_{50\%}$=−0.04 m;
ΔH$_{75\%}$=0.06 m;
ΔH$_{mean}$=0.03±0.27 m;
ΔH$_{25\%}$=−0.14 m;
ΔH$_{50\%}$=0.01 m;
ΔH$_{75\%}$=0.19 m;

Fig.10

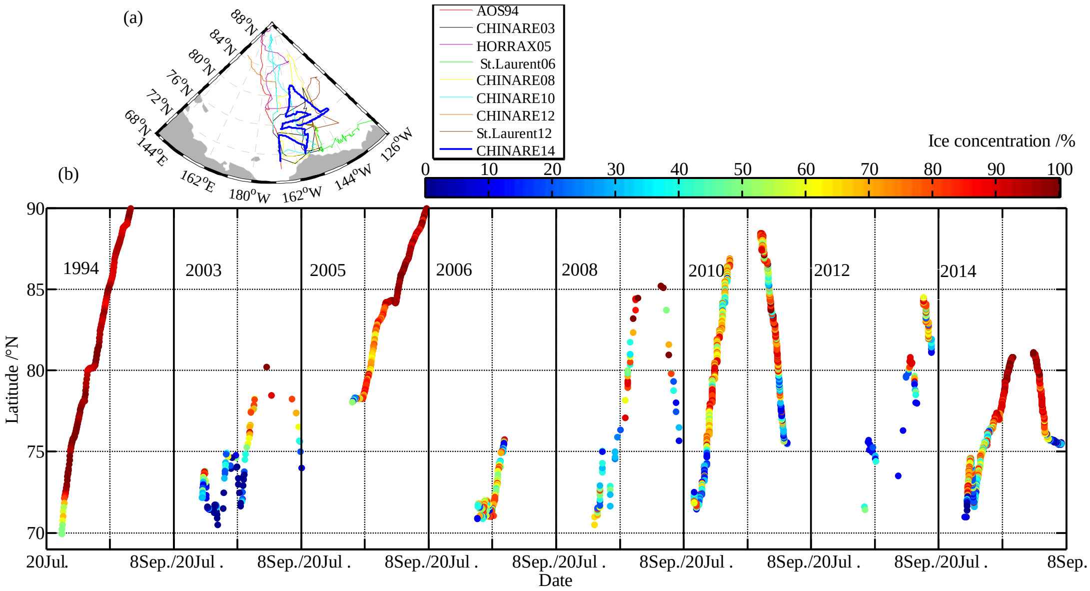
(a)
88°N
84°N
80°N
76°N
72°N
68°N
144°E
162°E
180°W
162°W
144°W
126°W
AOS94
CHINARE03
HORRAX05
St.Laurent06
CHINARE08
CHINARE10
CHINARE12
St.Laurent12
CHINARE14
(b)
Ice concentration /%
0
10
20
30
40
50
60
70
80
90
100
Latitude /°N
90
85
80
75
70
1994
2003
2005
2006
2008
2010
2012
2014
20Jul.
8Sep./20Jul .
8Sep.
Date

Fig.11

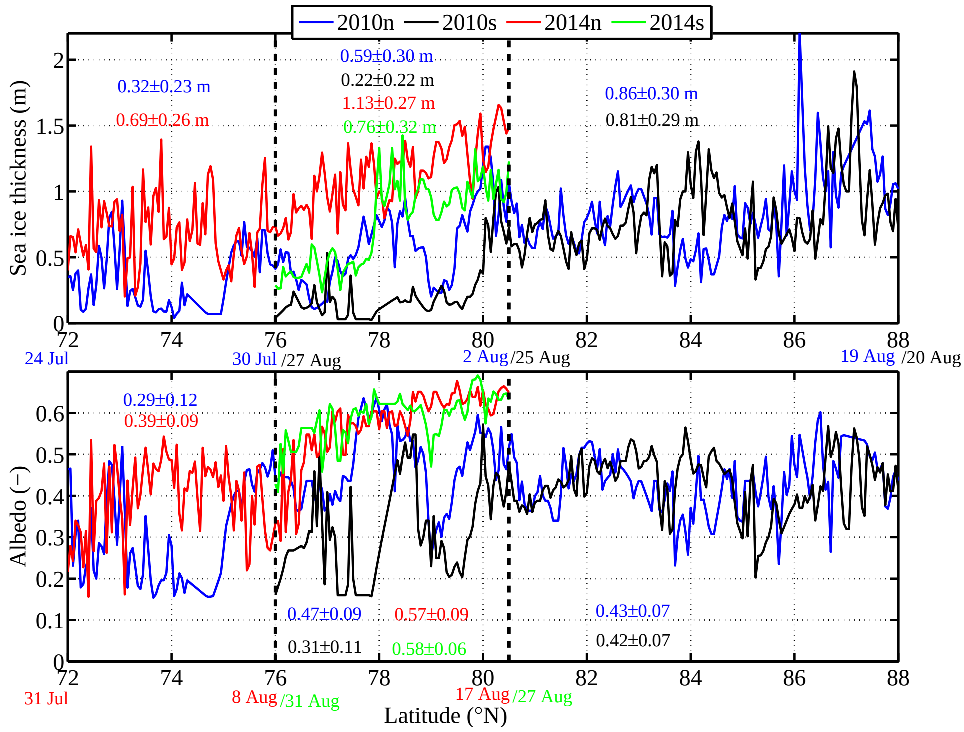

2010n
2010s
2014n
2014s
Sea ice thickness (m)
0.32±0.23 m
0.69±0.26 m
0.59±0.30 m
0.22±0.22 m
1.13±0.27 m
0.76±0.32 m
0.86±0.30 m
0.81±0.29 m
24 Jul
30 Jul /27 Aug
2 Aug/25 Aug
19 Aug /20 Aug
Albedo (−)
0.29±0.12
0.39±0.09
0.47±0.09
0.31±0.11
0.57±0.09
0.58±0.06
0.43±0.07
0.42±0.07
31 Jul
8 Aug /31 Aug
17 Aug /27 Aug
Latitude (°N)

Fig.12

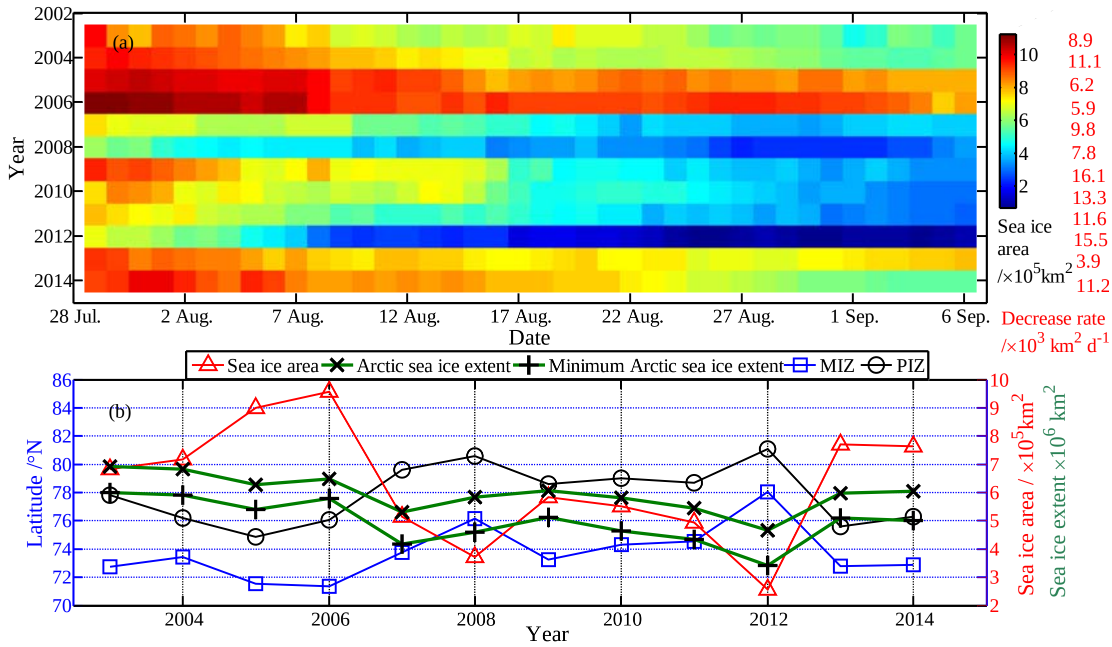

(a)
Year
2002
2004
2006
2008
2010
2012
2014
28 Jul.
2 Aug.
7 Aug.
12 Aug.
17 Aug.
22 Aug.
27 Aug.
1 Sep.
6 Sep.
Date
10
8
6
4
2
Sea ice area /×10^5 km^2
8.9
11.1
6.2
5.9
9.8
7.8
16.1
13.3
11.6
15.5
3.9
11.2
Decrease rate /×10^3 km^2 d^-1
Sea ice area
Arctic sea ice extent
Minimum Arctic sea ice extent
MIZ
PIZ
(b)
Latitude /°N
Sea ice area / ×10^5 km^2
Sea ice extent ×10^6 km^2
Year

Fig.13

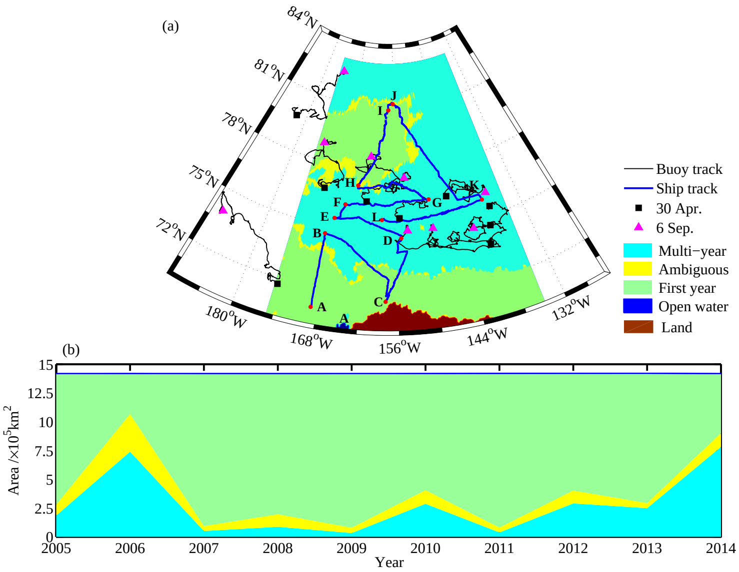

(a)
84°N
81°N
78°N
75°N
72°N
180°W
168°W
156°W
144°W
132°W
A
B
C
D
E
F
G
H
I
J
K
L
Buoy track
Ship track
30 Apr.
6 Sep.
Multi−year
Ambiguous
First year
Open water
Land
(b)
Area /×10^5km^2
15
12.5
10
7.5
5
2.5
0
2005
2006
2007
2008
2009
2010
2011
2012
2013
2014
Year

Fig.14

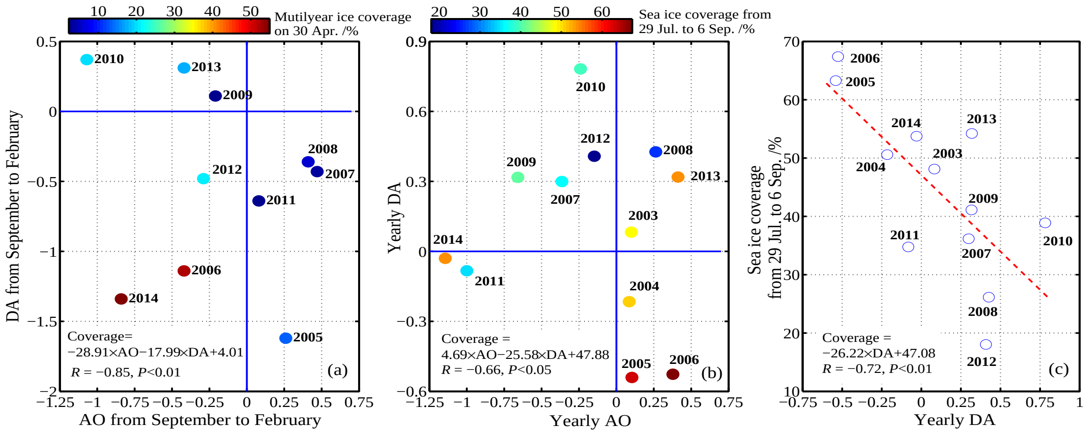

10 20 30 40 50
Mutilyear ice coverage on 30 Apr. /%
DA from September to February
AO from September to February
Coverage= −28.91×AO−17.99×DA+4.01
R = −0.85, P<0.01
(a)
20 30 40 50 60
Sea ice coverage from 29 Jul. to 6 Sep. /%
Yearly DA
Yearly AO
Coverage = 4.69×AO−25.58×DA+47.88
R = −0.66, P<0.05
(b)
Sea ice coverage from 29 Jul. to 6 Sep. /%
Yearly DA
Coverage = −26.22×DA+47.08
R = −0.72, P<0.01
(c)